nature communications

Article

https://doi.org/10.1038/s41467-025-58322-3

ACSS2 mediates an epigenetic pathway to regulate β-cell adaptation during gestation in mice

Received: 1 February 2024

Accepted: 12 March 2025

Published online: 20 May 2025

Check for updates

Yu Zhang[1,2,3,6], Shuang He[2,4,6], Xi Wang[2,3], Xin Wang[2,4], Mao-Yang He[3,4,5], Xin-Xin Yu[1,2,3] & Cheng-Ran Xu[1,2,3]

Maternal pancreatic β-cells undergo adaptive changes to meet the metabolic demands of pregnancy, and disruptions in this adaptation can lead to gestational diabetes mellitus. However, the mechanisms governing this adaptation remain largely unexplored. Using single-cell transcriptome combined with genetic analyses, we identified a precise process of β-cell adaptation in mice, characterized by progressive metabolic stress-related β-cell dysfunction, increased acetyl-CoA biosynthesis, and gene element-specific histone acetylation. STAT3 recruits p300 to promote histone acetylation of pregnancy-associated genes, a process enhanced by Acetyl-CoA Synthetase 2 (ACSS2). High-fat feeding induces hyperacetylation of chromatin regions specifically opened during pregnancy, leading to the overexpression of genes that impair β-cell function. However, these impairments can be rescued by β-cell-specific deletion of *Acss2*. Notably, ACSS2 is functionally implicated in the early establishment of β-cell adaptation in HFD-fed mice but does not appear to play a role in standard diet-fed mice until after the initiation of adaptation. Our study uncovers a finely regulated β-cell adaptation process at the single-cell level during pregnancy and identifies a specific epigenetic pathway that governs this process. These findings provide insights into β-cell plasticity and potential therapeutic strategies for gestational diabetes mellitus.

In response to environmental stress or stimuli, cells undergo physiological adaptation that is frequently reversible. However, when the adaptive response exceeds the limits of cellular tolerance, cell function is impaired, resulting in chronic diseases such as diabetes, fatty liver and cirrhosis, cardiac failure, and cancer. Animal models or human samples are employed to study the mechanisms of physiological and pathological cell adaptation. However, due to the lengthy duration of the adaptation process, these models or samples are inevitably influenced by variables such as energy metabolism, infection, inflammation, aging, and genetic background. Therefore, effective models are required to investigate cell adaptation from physiology to pathology.

During pregnancy, the number of β-cells and insulin secretion in maternal pancreatic islets increases to adapt to gestational insulin resistance[1,2]. Defective β-cell adaptation may lead to gestational diabetes mellitus (GDM)[3], which affects more than 10% of pregnant women worldwide, placing these women and their children are at high risk for long-term metabolic diseases and type 2 diabetes (T2D). The

[1]State Key Laboratory of Female Fertility Promotion, Department of Medical Genetics, School of Basic Medical Sciences, Peking University, Beijing 100191, China. [2]Peking-Tsinghua Center for Life Sciences, Peking University, Beijing 100871, China. [3]Academy for Advanced Interdisciplinary Studies, Peking University, Beijing 100871, China. [4]College of Life Sciences, Peking University, Beijing 100871, China. [5]PKU-Tsinghua-NIBS Graduate Program; Peking University, Beijing 100871, China. [6]These authors contributed equally: Yu Zhang, Shuang He. e-mail: cxu@pku.edu.cn

major risks for developing GDM include a high-calorie diet during pregnancy and obesity before pregnancy[4,5]. When pregnant mice on a C57BL/6 J background are fed a high-calorie diet, glucose intolerance results, suggesting impaired islet function[6]. Thus, pregnancy mice under dietary intervention may serve as a valid model to study the process and regulatory mechanisms of adaptive transition of β-cells from physiology to pathology, which remains largely unknown.

Several maternal and placental hormones, including prolactin, placental lactogens, and serotonin, act as extracellular signaling molecules that regulate gestational β-cell proliferation[7,8]. Upon binding to the prolactin receptor on the β-cell membrane, prolactin and placental lactogens activate the Janus kinase/signal transducers and activators of transcription (JAK-STAT) pathway[9,10]. Nonetheless, the intracellular regulatory mechanisms governing β-cell adaptation during pregnancy remain poorly understood. Several studies have employed RT–qPCR, microarray, and inDrop single-cell RNA-sequencing (scRNA-seq) approaches to assess gene expression patterns in whole islets from pregnant mice[11–14]. However, because islets contain multiple cell types and the sensitivity of these methods is limited, only a small fraction of commonly differentially expressed genes (DEGs) have been detected in these studies[2]. Thus, these studies provide only limited insight into the pathways and regulatory mechanisms underlying β-cell adaptation throughout gestation.

In this work, we employed multi-omics approaches to investigate the dynamic changes in pancreatic β-cells during pregnancy and the postpartum period in mice. We identified a regulatory mechanism linking metabolic stress to chromatin modifications that govern gene expression changes essential for β-cell adaptation. Through genetic analyses, we demonstrate that STAT3 interacts with p300 to modulate histone acetylation, with ACSS2 acting as a key metabolic sensor that influences this epigenetic process. Additionally, we found that high-fat diet (HFD) exposure during pregnancy alters chromatin accessibility, disrupting gene expression patterns critical for β-cell function. Importantly, β-cell-specific *Acss2* deletion mitigates these effects, preserving β-cell function under both HFD conditions and later stage standard diet (SD) conditions. These findings provide a mechanistic framework for understanding β-cell plasticity during pregnancy and highlight potential epigenetic targets for therapeutic intervention in gestational diabetes.

Results

β-cell specific adaptation during pregnancy

Previous studies have reported a significant upregulation in the proliferation of β-cells during pregnancy, particularly around the gestation day (G) 14.5 period[15,16]. To effectively characterize the state transitions of various types of endocrine cells within pancreatic islets during pregnancy, we performed high-throughput droplet-based 10x Genomics scRNA-seq on G14.5 and age-matched virgin (G0) mice (Supplementary Data 1). After filtering out low-quality cells and doublets, we obtained single cells expressing an average of 3,500 genes (Supplementary Fig. 1a, b). We then identified cell types using Louvain clustering and displayed on t-distributed stochastic neighbor-embedding (t-SNE). After excluding endothelial cells (*Pecam1*$^+$), mesenchymal cells (*Col3a1*$^+$), immune cells (*Fcgr1*$^+$), and ductal cells (*Spp1*$^+$), we obtained 7,774 *Neurod1*$^+$ endocrine cells, consisting of 5,427 β-cells (*Ins1*$^+$), 1,580 α-cells (*Gcg*$^+$), 572 δ-cells (*Sst*$^+$), and 195 PP-cells (*Ppy*$^+$) (Supplementary Fig. 1c-f). Interestingly, only β-cells among these endocrine lineages exhibited heterogeneous cell populations at the transcriptome level (Supplementary Fig. 1e-i). Previous studies have identified a substantial β-cell population with high *Glut2* expression (referred to as *Glut2*^{high} β-cells) and a small population with low *Glut2* expression (*Glut2*^{low} β-cells), accounting for 5-10% of all β-cells[17,18]. DEG analysis showed that each of these two populations exhibited pregnancy-associated transcriptomic heterogeneity and could be further divided into four cell populations (Supplementary Fig. 1g-i; Supplementary Data 1). The *Glut2*^{high} β-1 and *Glut2*^{low} β-1 cells predominated in G0 mice, whereas the *Glut2*^{high} β-2 and *Glut2*^{low} β-2 cells predominated in G14.5 mice (Supplementary Fig. 1e, g). Using cell cycle-related genes, we distinguished proliferative and quiescent β-cells and found that the proliferation rate of G14.5 β-cells was more than 10-fold higher than that of G0 β-cells (Supplementary Fig. 1j, k). Notably, other endocrine lineages did not show significant changes in proliferation rate between G0 and G14.5 (Supplementary Fig. 1l-n). Thus, our findings suggest that β-cells exhibit specific adaptation at the transcriptome level during pregnancy.

ScRNA-seq defines the β-cell adaptation process

To comprehensively understand the adaptation process of pancreatic β-cells during pregnancy, we applied a more sensitive well-based scRNA-seq approach, Smart-seq3xpress (Smart-seq3)[19], to islet cells from mice at G0, G3.5, G5.5, G6.5, G8.5, G10.5, G12.5, G14.5, G16.5, G18.5, postpartum (P) days P2, P7, and P14 with or without lactation (L or NL) (Fig. 1a, Supplementary Fig. 2a; Supplementary Data 2). A total of 3,481 β-cells passed quality control, and an average of 8,000 genes were detected per cell (Supplementary Fig. 2a-c). Batch effects between biological replicates at each time point were not significant (Supplementary Fig. 2d). Based on existing reports, we selected *Chgb*, *Ovol2*, and *Ttr* among the DEGs that exhibited gradual changes along the pseudotime[11–13] and validated the expression patterns of these genes in G0 and G14.5 β-cells using single cell RT–qPCR or immunofluorescence (Supplementary Fig. 2e-g).

We identified two cell clusters for both *Glut2*^{high} and *Glut2*^{low} β-cells throughout pregnancy using an unsupervised clustering method (Fig. 1b, Supplementary Fig. 3a). Both *Glut2*^{high}-1 and *Glut2*^{low}-1 β-cells were predominant in G0, early gestation mice, and postpartum days with lactation, whereas *Glut2*^{high}-2 and *Glut2*^{low}-2 β-cells were present in mid- and late-gestation mice, and postpartum days with lactation (Fig. 1b, Supplementary Fig. 3b, c). In *Glut2*^{high} β-cells, principal component analysis (PCA) showed that the majority of β-cells were aligned along the PC2 axis, whereas a minor proportion of β-cells were segregated along the PC1 axis (Supplementary Fig. 3d). Gene Ontology (GO) analysis showed that PC1-related genes were enriched in terms such as “chromosome segregation” and “DNA replication” (Supplementary Fig. 3e; Supplementary Data 3), indicating that the cells distributed along the PC1 axis were proliferative cells. The percentage of proliferative β-cells peaked at G14.5, as validated by immunofluorescence analysis of Ki67, a marker of proliferative cells (Supplementary Fig. 3f, g).

We performed a second round of PCA excluding cell cycle-related genes. The gravity center of the cell distribution region was calculated for each time point, and each region was circled on the PCA plot. These centers were utilized to determine the regression line reflecting the path of cell state change (Fig. 1c). The distance from the beginning of the line to the projection of each cell on the line was calculated as the pregnancy-associated pseudotime value. Then, we aligned *Glut2*^{high} β-cells in pseudotime and discovered that at the transcriptome level, β-cell adaptation began as early as G6.5, progressed steadily, and peaked at G18.5 but recovered postpartum (Fig. 1d). Curiously, the β-cells of nonlactating mice abruptly reverted to a near nonpregnant state as early as P2, whereas those in lactating animals recovered more slowly (Fig. 1d), suggesting that the gestational state is stimulated and maintained by signals associated with pregnancy and lactation (e.g., prolactin)[20].

Hierarchical clustering revealed that, excluding cell cycle-related genes, the 769 genes with variable expression throughout gestation were classified into two clusters (Fig. 1e; Supplementary Data 4). Cluster-a genes were upregulated during pregnancy and enriched in the Kyoto Encyclopedia of Genes and Genomes (KEGG) and GO terms endoplasmic reticulum (ER) stress response[21,22], unfolded protein

https://doi.org/10.1038/s41467-025-58322-3

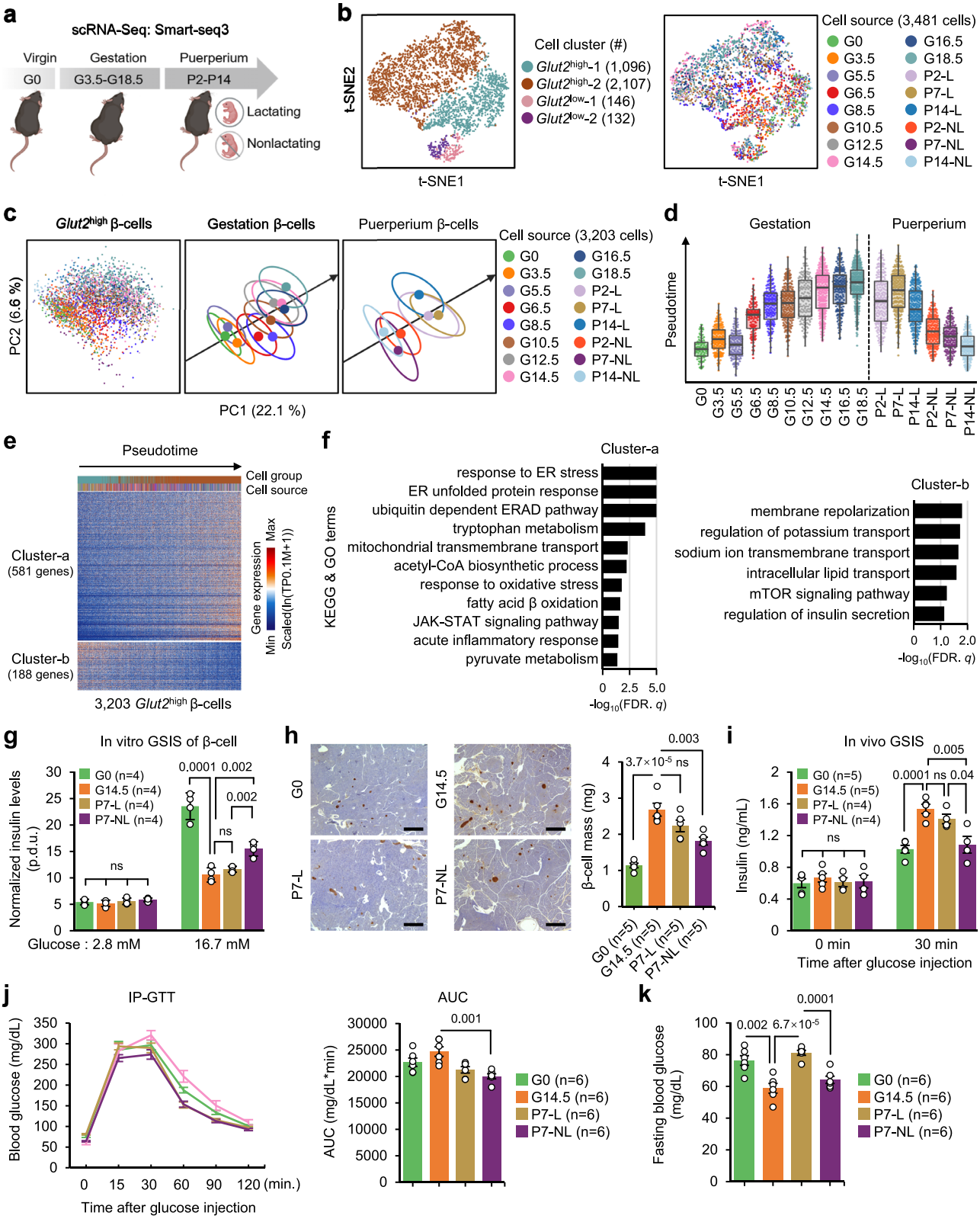

response (UPR)[23], oxidative stress and acute inflammatory responses[24], suggesting that metabolic stress in β-cells is aggravated during pregnancy. Additionally, metabolic processes such as fatty acid β-oxidation, acetyl-CoA biosynthesis, and amino acid and pyruvate metabolism, which are associated with acetyl-CoA production[25], as well as the JAK-STAT signaling pathway[9], were enriched among cluster-a genes (Fig. 1f; Supplementary Data 3). The downregulated cluster-b genes were enriched in terms related to β-cell functions, such as ion transport and insulin secretion (Fig. 1f; Supplementary Data 3). Interestingly, despite the upregulation of downstream targets mTOR, such as *Akt1*, *Gsk3b*, and *Eif4ebp1*, known to be associated with β-cell proliferation[26,27], the mTOR signaling pathway was enriched in cluster-b genes (Supplementary Fig. 3h). Notably, the number of genes in cluster-a was three times higher than that in cluster-b (Fig. 1e). The dynamic patterns of both clusters indicate reduced β-cell function during pregnancy.

Fig. 1 | β-cell adaptation process during pregnancy at the single-cell level. **a** Schematic workflow for Smart-seq3 scRNA-seq on β-cells from virgin, pregnant, and postpartum mice. Illustration created with BioRender (BioRender.com/r42u304). **b** t-SNE plots showing the cell cluster (left) and cell source (right) of β-cells. Each dot represents a single cell. Cell group and source are color coded. Cell counts are denoted within brackets. **c** PCA plot of *Glut2*^{high} β-cells identified in panel (**b**) (left). Each dot represents the gravity center for the distribution of cell for each source (circled) (middle and right). **d**, Box scatter plots showing the cells in each *Glut2*^{high} β-cell population at different times during pregnancy, arranged by pseudotime value. Box plots display the median (middle line), 25th-75th percentiles (box), whiskers extending 1.5 times the interquartile range from the edges, minimum and maximum values at whisker ends. Biological replicates of different times refer to Supplementary Fig. 2d. **e** Heatmap showing the variably expressed genes identified in *Glut2*^{high} β-cells. Each column represents a single cell, ordered by pseudotime value. Each row represents a gene. The color scheme is the same as in panel (**b**). **f** Representative enriched GO and KEGG terms in gene clusters identified in panel (**e**). One-sided Kolmogorov-Smirnov test. FDR: false discovery rate. **g** In vitro GSIS levels of Ins1-RFP^{+} β-cells in mouse pancreatic islets. p.d.u. represents procedure-defined unit. **h**, Immunohistochemistry for insulin (brown) shows β-cell area in pancreatic sections (left). Scale bar = 1 mm. Statistics of the β-cell mass in each mouse pancreas (right). Eight sections at 100 μm intervals were measured for each pancreas sample. **i**, In vivo GSIS levels of mice before and 30 min after glucose injection. **j**, IP-GTT levels in fasted mice after glucose injection (left). Quantification of the areas under the curve (AUC) (right). **k**, Fasting (0 min.) blood glucose levels of mice in panel (**j**). Data in (**g**–**k**) are presented as mean ± SEM, and an unpaired two-tailed t-test was used to compare two groups. The numbers in the plot indicate the p-value. n represents the number of mice. Source data (**g**–**k**) are provided as a Source Data file.

To provide an accurate representation of insulin secretion capability on a per β-cell basis, the in vitro glucose-stimulated insulin secretion (GSIS) levels of islets were normalized by β-cell number (Ins1-RFP^{+} cells) by utilizing the *Ins1-RFP* transgenic mouse strain[28]. Given the observable initial recovery in P7-NL, in contrast to the absence of recovery in P7-L, we selected to assess the functionality changes of β-cells from G0, G14.5, P7-NL, and P7-L mice. The in vitro GSIS function of islet β-cells was considerably reduced at G14.5 compared to G0 and slightly restored in P7-NL but not in P7-L mice (Fig. 1g). However, the β-cell mass significantly increased in G14.5, then decreased in P7-NL but not in P7-L mice (Fig. 1h). Thus, the in vivo GSIS data displayed a significant increase in overall insulin secretion levels in mice at G14.5 (Fig. 1i). Consistently, the intraperitoneal glucose tolerance test (IP-GTT) results showed that the glucose tolerance in mice only exhibited slight fluctuation throughout gestation and postpartum (Figs. 1j), and G14.5 mice even exhibited lower fasting blood glucose level compared to G0 and P7-L, but not P7-NL mice (Fig. 1k). These findings suggest that the impaired β-cell secretory capacity during pregnancy was compensated by an elevated β-cell mass to maintain glucose homeostasis[29].

In conclusion, single-cell analysis reveals a β-cell state transition during pregnancy characterized by dynamic expression changes in a large number of genes, a decrease in β-cell function, and an increase in the proliferation rate of β-cells.

The alterations in *Glut2*^{low} β-cells were comparable to those in *Glut2*^{high} β-cells during pregnancy (Supplementary Fig. 3i, j; Supplementary Data 4). Despite most genes with variable expression being common to both populations, *Glut2*^{high} β-cells underwent a more significant transcriptomic adaptation than *Glut2*^{low} β-cells during pregnancy (Fig. 1e; Supplementary Fig. 3j, k). Additionally, the ratio of *Glut2*^{low} to *Glut2*^{high} β-cells remained steady at all time points (Supplementary Fig. 3l). To avoid interference from cellular heterogeneity, subsequent single-cell analyses were concentrated on the *Glut2*^{high} population, which comprises the vast majority of β-cells.

Increased histone acetylation during pregnancy

Given that the upregulated gene cluster included terms related to acetyl-CoA biosynthesis process (Fig. 1f), we utilized liquid chromatography with tandem mass spectrometry (LC-MS/MS) to confirm this phenomenon. We found that G14.5 islets contained more acetyl-CoA than G0 islets (Fig. 2a). Since acetyl-CoA is a substrate for histone acetyltransferases[30], we examined global histone acetylation levels by Western blotting. Our results showed that pan-acetylated histone H3 (acH3), H3K27ac, and H3K9ac were elevated during pregnancy (Fig. 2b). Immunostaining further confirmed the elevated H3K27ac levels in β-cells at G14.5 (Supplementary Fig. 4a). To investigate the relationships among histone acetylation, chromatin structure, and gene regulation, we performed CUT&RUN[31] of an activating histone mark (H3K27ac) and ATAC-seq on RFP^{+} G0, G14.5, and P7-NL β-cells derived from an *Ins1-RFP* mouse and isolated using fluorescence-activated cell sorting (FACS) (Supplementary Fig. 4b-d). We also included a histone mark related to enhancer elements (H3K4me1) and a repressive mark (H3K27me3) in our study (Supplementary Fig. 4c).

Globally, 1,510 H3K27ac peaks were higher in β-cells at G14.5 than at G0, while 709 peaks were lower (Fig. 2c). The H3K27ac levels in P7-NL β-cells were restored to even lower than those in G0 β-cells (Supplementary Fig. 4e), consistent with the upregulation of several histone deacetylase genes in β-cells at P7-NL compared to G14.5 (Supplementary Fig. 4f). These results revealed that H3K27ac levels were significant upregulated during pregnancy but downregulated post-delivery without lactation. Similarly, G14.5 β-cells exhibited more open chromatin, with reduced accessibility at only a few loci, relative to G0 and P7-NL β-cells (Fig. 2d, Supplementary Fig. 4g). Additionally, the signal intensities of ATAC-seq related to the 1,510 upregulated H3K27ac CUT&RUN peak loci (Fig. 2c) were also generally upregulated in G14.5 β-cells relative to G0 β-cells (Supplementary Fig. 4h). In G14.5 β-cells, both the enhancer and promoter loci of cluster-a genes (Fig. 1e) were associated with an increase in H3K27ac modification and more accessible local chromatin (Fig. 2e). The cluster-b genes (Fig. 1e) had higher H3K27ac levels than cluster-a genes in G0 β-cells and showed a slight decrease in H3K27ac levels during pregnancy, but their ATAC-seq signal intensity remained increased (Fig. 2e). This observation indicates that the downregulation of the cluster-b genes during pregnancy is not regulated by reduced chromatin accessibility. Another enhancer-associated histone mark, H3K4me1, displayed a pattern similar to that of H3K27ac at enhancer regions but was absent from promoter regions (Fig. 2e). Notably, H3K27me3 signals remained steady during pregnancy (Supplementary Fig. 4i). These results suggest that the elevated H3K27ac levels contribute to β-cells adaptation by regulating chromatin accessibility and gene expression levels in relevant gene regions.

In conclusion, these findings demonstrated a positive relationship between increased intracellular acetyl-CoA and increased histone acetylation, which may modulate transcriptome dynamics during pregnancy.

The histone acetyltransferase p300 promotes β-cell adaptation

To determine whether the acetyltransferase p300 regulates histone acetylation in β-cells during pregnancy, we performed p300 CUT&RUN on G0, G14.5, and P7-NL β-cells (Fig. 3a, Supplementary Fig. 5a, b). The analysis revealed significantly stronger p300 signals in promoter and enhancer regions of G14.5 β-cells compared to G0 and P7-NL β-cells, suggesting a specific regulatory role for p300 at this stage (Fig. 3a). In each cell population, the binding sites of p300 overlapped with those of H3K27ac by approximately 80% (Fig. 3b).

To mimic the β-cell adaptation during gestation, we treated islets from non-pregnant mice in vitro with human maternal serum (MS) from women in their third trimester (> 28 weeks). Islets treated with normal serum (NS) from age-matched women served as a control. Additionally, to validate the role of p300 in regulating the β-cell adaptation process, we treated islets with A485, an inhibitor of p300

https://doi.org/10.1038/s41467-025-58322-3

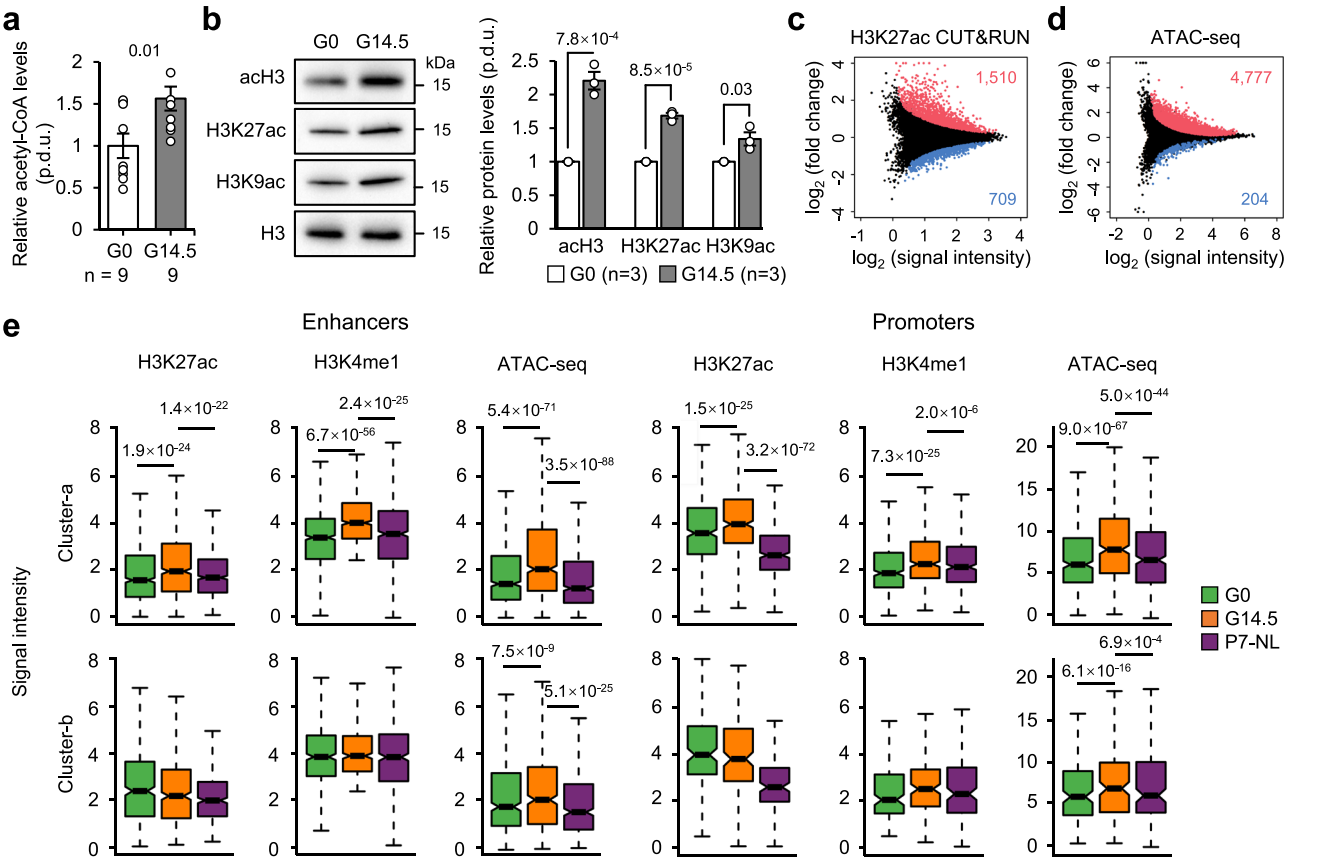

Fig. 2 | Dynamics of histone acetylation in β-cells during pregnancy. **a** Quantification of relative acetyl-CoA levels in islets from G0 and G14.5 mice measured by LC–MS/MS. n indicates the number of biological replicates. **b**, Western blot images of islets from G0 and G14.5 mice obtained using the conventional Western blotting approach (left). Quantification of Western blot signals calculated by ImageJ software (right). **c, d** Comparison of genome-wide H3K27ac (**c**) or ATAC-seq (**d**) levels between G0 and G14.5 β-cells. The number of dots represents significantly increased signals of H3K27ac CUT&RUN (**c**) or ATAC-seq (**d**) peaks in G14.5 (red) and G0 (blue) β-cells. p-value ≤ 0.05 (**c**). *p* value ≤ 0.2 (**d**). Two-sided moderated t-test. **e** Signal intensity of H3K27ac, H3K4me1, and ATAC-seq at the enhancer elements (left) or the promoter elements (right) of cluster-a genes (upper) or cluster-b genes (bottom) (see Fig. 1e) in G0, G14.5, and P7-NL β-cells. Paired two-sided Wilcoxon rank-sum test. Box plots display the median (middle line), 25th–75th percentiles (box), whiskers extending 1.5 times the interquartile range from the edges, minimum and maximum values at whisker ends. 2 biological replicates were performed (refer to Supplementary Fig. 4c). Data in (**a, b**) are presented as mean ± SEM, and an unpaired two-tailed t-test was used to compare two groups. n indicates the number of biological replicates. The numbers in the plot indicate p-value. Source data (**a, b**) are provided as a Source Data file.

acetyltransferase activity, in this in vitro islet model[32]. After four days of culture, islet morphogenesis appeared normal (Fig. 3c). We performed scRNA-seq on cells from different culture conditions. To avoid the inherent differences between in vivo and in vitro systems, we projected them onto the PCA plot in Fig. 1c to calculate their pregnancy-associated pseudotime values (Fig. 3d, e, Supplementary Fig. 5c, d; Supplementary Data 2). When single cells from each condition were aligned according to pseudotime value, we discovered that MS induced pregnancy-associated β-cell adaptation (Fig. 3d, e, Supplementary Fig. 5e; Supplementary Data 2).

Additionally, cells treated with MS exhibited increased levels of histone H3K27ac at sites where H3K27ac was elevated during pregnancy compared to cells treated with NS (Fig. 2c, Supplementary Fig. 5f-h). Considering that prolactin serves as an extracellular signal inducing adaptive changes in β-cells during pregnancy, we investigated it effects in combination with NS. We observed that prolactin significantly increases H3K27ac levels, underscoring the regulatory role of prolactin-related signaling pathways in histone modification during β-cell adaptation (Supplementary Fig. 5i). Furthermore, both MS and prolactin induced serotonin production by islet β-cells (Supplementary Fig. 5j). These results demonstrated that this culture system could simulate the pregnancy-related β-cell adaptation process in vitro. Notably, A485 treatment significantly impeded this adaptation process (Fig. 3e). On a PCA plot of scRNA-seq data from the cultured β-cells, the MS-induced adaptation process formed a line, while a segregated pathway was distinguished from the pregnancy-associated β-cell adaptation trajectory (Supplementary Fig. 5k). The variable genes related to the segregated pathway were associated with β-cell dysfunction (Supplementary Fig. 5l, m; Supplementary Data 3, 4). Ki67 immunostaining revealed a marked increase in β-cell proliferation within the MS culture compared to the NS culture. However, co-treatment with A485 significantly inhibited MS-induced β-cell proliferation (Fig. 3f).

To investigate p300 function in vivo, we knocked out *p300* in β-cells (abbreviated *p300*βKO) with a conditional *p300* allele[33] in a *Pdx1-Cre*^{ER} mouse strain[34] in an *Ins1-RFP* background. Tamoxifen was administered for one week, and then the mice were mated (Fig. 3g). Bulk-cell RT–qPCR confirmed significant knockout efficiency of *p300* (Supplementary Fig. 6a). ScRNA-seq was performed on β-cells from *p300*βKO and wild-type (WT) littermate controls at G0 and G14.5 (Fig. 3g, Supplementary Fig. 6b, c; Supplementary Data 2), and the resulting data were visualized on PCA and diffusion map plots (Supplementary Fig. 6d). On the PCA plot, the gravity centers of the G0 and G14.5 WT cell distribution regions were calculated to determine the regression line of the pregnancy-related pathway; the pregnancy-associated pseudotime values were defined on the basis

https://doi.org/10.1038/s41467-025-58322-3

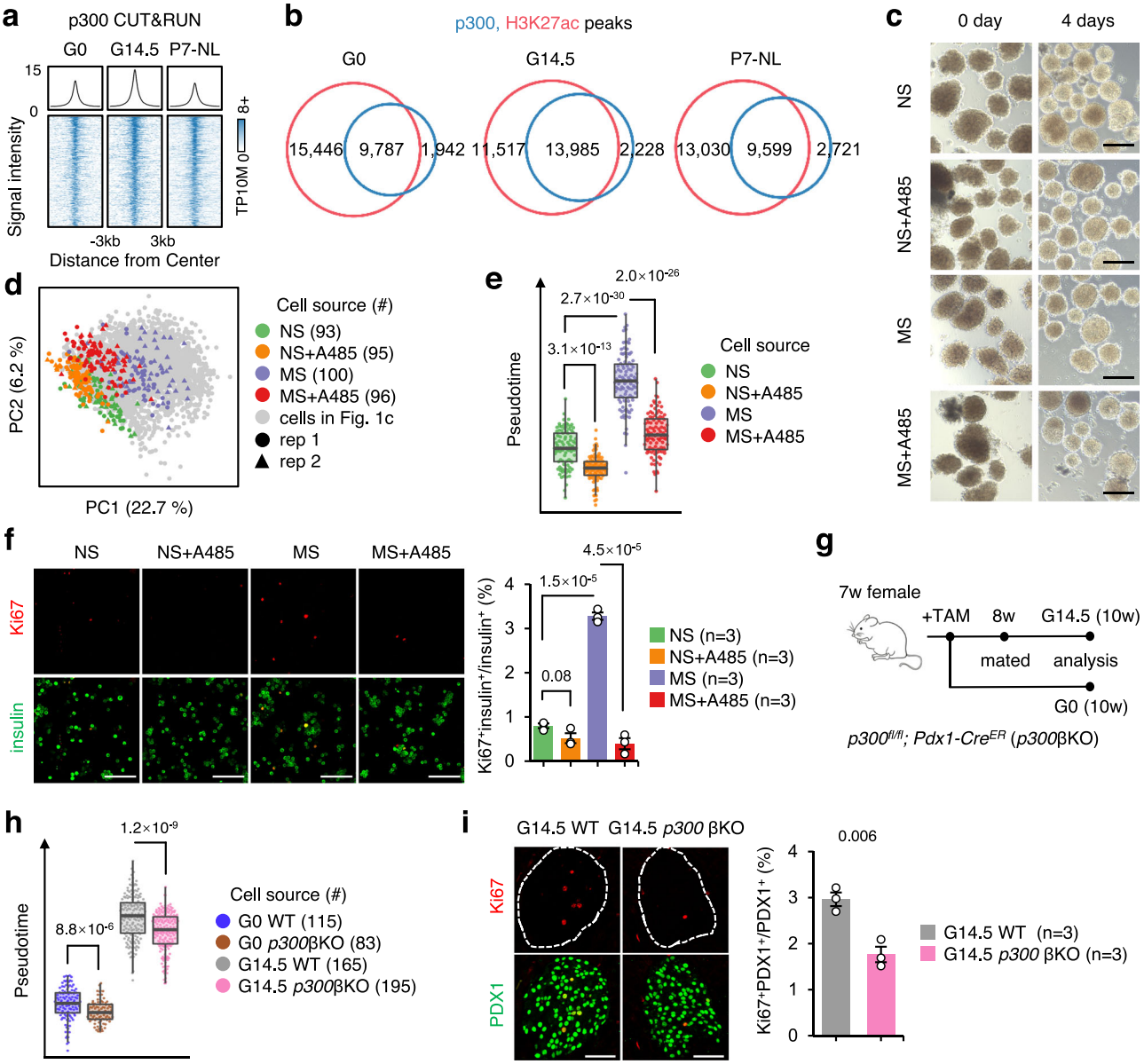

Fig. 3 | The histone acetyltransferase p300 promotes β-cell adaptation. **a** Composite plots (upper) and signal intensity (bottom) of p300 CUT&RUN in the promoter and enhancer regions in G0, G14.5, and P7-NL β-cells. **b** Overlap of p300 and H3K27ac binding sites in β-cells from distinct time points. **c** Islet morphology before and after culture under different conditions. Scale bar = 100 μm. A485 concentration: 5 μM. MS represents human maternal serum from women in the third trimester (> 28 weeks), and NS represents normal serum from age-matched women. 3 biological replicates were performed. **d** PCA plot showing the cultured single β-cells projected onto the plot in Fig. 1c. Each dot represents a single cell. The circles and triangles represent independent biological replicates. rep: biological replicates. **e** Box scatter plots showing β-cells cultured under different conditions arranged by pregnancy-associated pseudotime values. Each dot represents a single cell. Unpaired two-sided Wilcoxon rank-sum test. **f** Immunostaining of Ki67 and insulin expression in islet cells after 4 days of culture (left). Scale bar = 100 μm. Quantification of the percentage of Ki67$^+$insulin$^+$ cells among all insulin$^+$ β-cells (right). n represents the biological replicates. More than 1,000 insulin$^+$ cells were counted for each replicate. **g** Schematic of the workflow for the generation of pregnant *p300*βKO mice. TAM tamoxifen. **h**, Box scatter plots showing β-cells from different mouse samples arranged by pseudotime values. Unpaired two-sided Wilcoxon rank-sum test. **i** Immunofluorescence images of Ki67 and PDX1 in pancreatic tissue sections (left). Scale bar = 50 μm. Quantification of Ki67$^+$PDX1$^+$ cells among all PDX1$^+$ β-cells in each tissue (right). n represents the number of mice. Box plots in (**e**, **h**) display the median (middle line), 25th–75th percentiles (box), whiskers extending 1.5 times the interquartile range from the edges, minimum and maximum values at whisker ends. Data in (**f**, **i**) are presented as mean ± SEM, and an unpaired two-tailed t-test was used to compare two groups. Source data (**f**, **i**) are provided as a Source Data file.

of this regression line (Supplementary Fig. 6d, e; refer to Methods). By aligning the β-cells from the mouse samples according to pseudotime values, we found that the progress of β-cells from G14.5 *p300*βKO mice along the pregnancy-related pathway lagged behind that of G14.5 WT mice (Fig. 3h, Supplementary Fig. 6d). Notably, the phenotype of β-cells in the A485 culture system was more pronounced than that of *p300*βKO β-cells in vivo (Fig. 3e, h), suggesting that other histone acetyltransferase, such as CBP[32], which can also be inhibited by A485, may participate in the regulation of β-cell adaptation.

Additionally, a segregated pathway was distinguished from the pregnancy-associated β-cell adaptation pathway (Supplementary Fig. 6d). The genes downregulated in this pathway (cluster-1) were related to the regulation of β-cell functions, while the upregulated genes (cluster-2) were associated with metabolic stress (Supplementary Fig. 6f, g; Supplementary Data 3, 4). Immunostaining for Ki67

revealed a reduced β-cell proliferation rate in *p300*βKO mice at G14.5 (Fig. 3i), which may attribute to a decrease in β-cell mass (Supplementary Fig. 6h). Consistently, impaired in vivo GSIS and GTT were observed in G14.5 *p300*βKO mice (Supplementary Fig. 6i, j).

In summary, these findings demonstrate that p300 is essential for β-cell adaptation and expansion during pregnancy. By regulating histone acetylation and β-cell functional genes, p300 ensures the effective response of β-cells to the metabolic demands of pregnancy.

STAT3 deficiency has no early effect on β-cell adaptation in SD-fed mice but affects β-cells at later stages of pregnancy

To identify potential factors mediating the establishment of particular local H3K27ac contexts, we performed motif enrichment analysis of the CUT&RUN data. The analysis revealed that the most abundant binding motif in the regulatory regions with elevated H3K27ac and p300 during gestation was associated with STAT family transcription factors (TFs) (Fig. 4a, Supplementary Fig. 7a; Supplementary Data 5). Although STAT5 is a major mediator of multiple signaling pathways in islets, including prolactin and growth hormone pathways[35], β-cell-specific knockout of the *Stat5a/b* gene had minimal effect on glucose homeostasis during gestation[36], suggesting the presence of compensatory factors. Gene expression analysis revealed that *Stat3* was the most abundantly expressed member of the STAT family in β-cells, and the level of phosphorylated STAT3 (Ser727) was higher in G14.5 β-cells compared to G0 β-cells (Fig. 4a, b).

To further explore the role of STAT3, we performed STAT3 CUT&RUN in G0, G14.5, and P7-NL β-cells (Supplementary Fig. 7b). STAT3 was the most enriched binding motif, confirming the reliability of the CUT&RUN data (Supplementary Fig. 7c; Supplementary Data 5). Surprisingly, in G14.5 β-cells, 67% of the STAT3 binding sites were also occupied by p300 (Fig. 4c). These cobinding sites included 2,888 locations where p300 signals were elevated (Fig. 4d). Notably, these sites also exhibited increased H3K27ac binding in G14.5 β-cells (Fig. 4e). The interaction between STAT3 and p300 was validated by a coimmunoprecipitation assay in G14.5 islets (Fig. 4f). Comparing G14.5 to G0 β-cells revealed that the loci with enhanced STAT3 binding during pregnancy also showed increased intensity of H3K27ac and p300 binding (Supplementary Fig. 7d-f). Furthermore, these sites returned to the nonpregnant state in P7-NL β-cells (Supplementary Fig. 7d-f). All these results suggest that STAT3 collaborates with p300 to regulate the dynamics of histone acetylation during β-cell adaptation.

Similar to the approach taken to conditionally knock out *p300*, we used the *Pdx1-Cre*^{ER} mouse strain to delete *Stat3*[37] in β-cells (abbreviated *Stat3*βKO) in an *Ins1-RFP* background and validated the mutation by immunofluorescence with an anti-STAT3 antibody (Fig. 3g, Supplementary Fig. 7g). ScRNA-seq analysis of β-cells from *Stat3*βKO and WT littermates at G0, G14.5, and G18.5 showed subtle transcriptomic differences at G0 and G14.5, but more pronounced changes at G18.5 (Supplementary Fig. 7h, i; Supplementary Data 2, 4). A pregnancy-associated trajectory was fitted on PCA and diffusion map plots, which showed that β-cells from G18.5 *Stat3*βKO mice lagged compared to those from G18.5 WT mice (Fig. 4g, Supplementary Fig. 7j, k). Ki67 immunostaining revealed a reduced β-cell proliferation rate in both G14.5 and G18.5 *Stat3*βKO mice (Fig. 4h). Correspondingly, *Stat3*βKO mice displayed a marked inhibition of β-cell mass expansion during gestation (Fig. 4i). Although the in vitro GSIS levels of β-cell in G18.5 *Stat3*βKO islets showed a slight increase, *Stat3*βKO mice exhibited reduced in vivo GSIS levels compared to WT mice during gestation (Fig. 4j, Supplementary Fig. 7l). Consistently, we observed a modest increase in the area under the curve (AUC) of GTT levels in *Stat3*βKO mice at G18.5, but not in nonpregnant G0 and P21-L mice (Supplementary Fig. 7m). These results suggest that during pregnancy, *Stat3*βKO impeded the β-cell adaptation process but slightly protected β-cell function. However, this protection may not be sufficient to compensate for the reduction in β-cell mass. In addition, CUT&RUN showed a global decrease in H3K27ac levels in G18.5 *Stat3*βKO β-cells compared with G18.5 WT β-cells (Fig. 4k, Supplementary Fig. 8a), including at both cluster-a and cluster-b genes (Fig. 1e, Supplementary Fig. 8b, c). These findings demonstrated that STAT3 is essential for the adaptation and expansion of β-cells during pregnancy.

Furthermore, we assessed the function of the STAT protein in the islet culture system described above using the small molecule nifuroxazide, a potent inhibitor that broadly targets STAT1/3/5. First, we confirmed that both MS and prolactin alone induced elevated levels of phosphorylated STAT3 (Ser727) protein in cultured islets (Fig. 4l). When projected onto the PCA plot of the pregnancy trajectory, nifuroxazide-treated β-cells exhibited a more delayed process than nontreated β-cells (Fig. 4m, Supplementary Fig. 8d-f; Supplementary Data 2). A segregated pathway was distinguished from the pregnancy-associated β-cell adaptation pathway (Supplementary Fig. 8g). Genes related to this pathway were associated with the maintenance of β-cell functions (Supplementary Fig. 8h, i; Supplementary Data 3, 4). Ki67 immunostaining showed increased proliferation of β-cells in MS culture but not in MS culture with nifuroxazide cotreatment (Supplementary Fig. 8j).

Collectively, these findings suggest that STAT3 collaborates with p300 to regulate histone acetylation dynamics during pregnancy. While STAT3 may not play a pivotal role at G14.5, its importance becomes more pronounced at later stages, particularly at G18.5, where its deficiency significantly disrupts β-cell adaptation and mass expansion.

ACSS2 promotes β-cell adaptation by regulating histone acetylation at later stages of pregnancy

The rapid increase in histone acetylation is dependent on the intracellular acetyl-CoA content[29,38]. We found that ACSS2 an acetate-dependent nuclear acetyl-CoA synthetase[39], was upregulated at the gene and protein levels in β-cells during pregnancy (Fig. 5a-c, Supplementary Fig. 9a). Immunostaining revealed that ACSS2 was predominantly localized in the nuclei of β-cells but not in α-cells (Fig. 5c).

To investigate the function of ACSS2 in gestational β-cell adaptation, we generated a mouse strain with a conditional *Acss2* knockout allele flanked by LoxP sites in exons 3-7 (Fig. 5d). Using the same strategy as described previously (Fig. 3g), we eliminated *Acss2* in β-cells (abbreviated *Acss2*βKO), confirmed by immunofluorescence using an anti-ACSS2 antibody (Supplementary Fig. 9b). ScRNA-seq was conducted on G0, G14.5, and G18.5 β-cells from *Acss2*βKO and WT mice (Supplementary Fig. 9c, d; Supplementary Data 2). DEG analysis showed no or subtle differences between WT and *Acss2*βKO β-cells at G0 or G14.5 (Supplementary Fig. 9e; Supplementary Data 4). However, we identified 161 downregulated genes and 390 upregulated genes in G18.5 *Acss2*βKO β-cells compared to G18.5 WT β-cells (Fig. 5e, Supplementary Fig. 9e; Supplementary Data 4). PCA and diffusion map plots showed that the G0 β-cells from WT and *Acss2*βKO mice were in the same cell cluster, whereas G18.5 WT and *Acss2*βKO cells exhibited segregated distributions, indicating that *Acss2* deletion significantly inhibited the β-cell adaptation process, suggesting that ACSS2 plays a more prominent role in later stages of pregnancy, as measured by the pregnancy-associated cell trajectory coordinates at G18.5 (Fig. 5f, Supplementary Fig. 9f).

The downregulated or upregulated genes in *Acss2*βKO β-cells were upregulated and downregulated, respectively, during normal pregnancy (Fig. 5e). GO analysis showed that the downregulated genes were related to ER stress, and the upregulated genes, including TFs *Nr1d1, Rfx6, Pdx1, Nkx6.1*, and *Neurod1*, were related to the regulation of β-cell functions such as glucose homeostasis, exocytosis, and insulin secretion[40–42] (Fig. 5e, g, Supplementary Fig. 9g, h; Supplementary Data 3). Notably, crucial genes associated with glucose uptake, metabolism, and mitochondrial function were upregulated in G18.5

https://doi.org/10.1038/s41467-025-58322-3

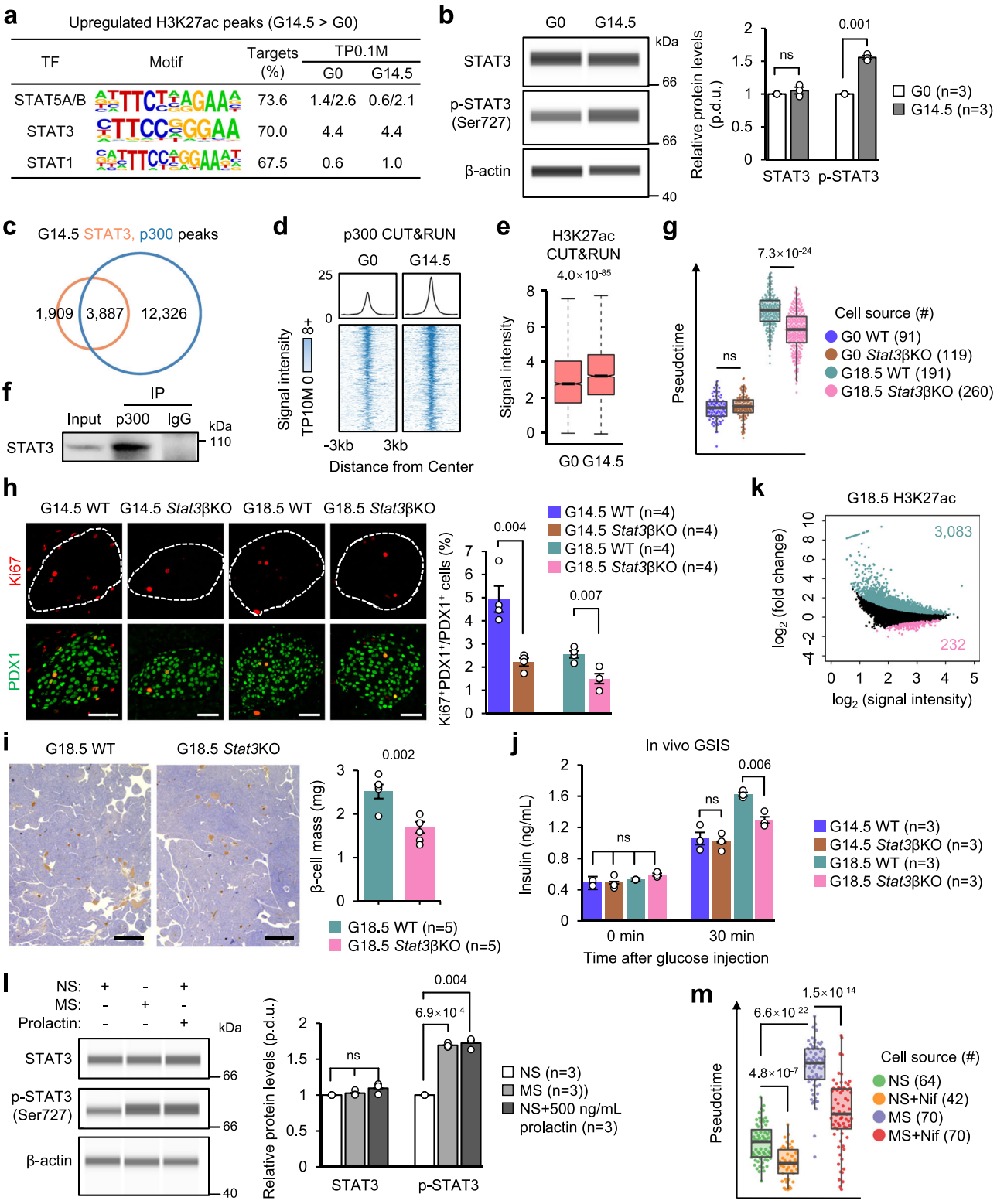

*Acss2*βKO β-cells (Supplementary Fig. 9g; Supplementary Data 3). These results suggested that *Acss2* deficiency may elevate β-cell functions during pregnancy. Indeed, we found that the in vitro GSIS levels of β-cells were significantly increased in *Acss2*βKO mice islets compared with WT mice at G18.5, but not at nonpregnant G0 mice (Fig. 5h). Ki67 immunostaining showed that β-cell proliferation in *Acss2*βKO mice remained comparable to that in WT mice at both G14.5 and G18.5 (Fig. 5i). Correspondingly, the β-cell mass levels were comparable between WT and *Acss2*βKO mice at G18.5 (Fig. 5j). The in vivo GSIS levels were increased in G18.5 *Acss2*βKO mice (Fig. 5k). Additionally, the AUC of GTT levels were slightly decreased in *Acss2*βKO mice at G18.5, but remained comparable to WT mice at G0 and P21-L (Supplementary Fig. 9i). These findings demonstrate that *Acss2*βKO β-cells effectively maintain normal glucose homeostasis during pregnancy.

We further tested whether ACSS2 regulates histone acetylation by measuring the H3K27ac modification levels in G18.5 WT and *Acss2*βKO β-cells (Supplementary Fig. 9j). We found that global H3K27ac binding

Fig. 4 | STAT3 interacts with p300 to regulate β-cell adaptation during pregnancy. a Top three motifs enriched at the putative enhancers with increased H3K27ac marks in G14.5 β-cells compared to G0 β-cells. **b** Immunoblot assays of Ins1-RFP$^+$ β-cells (left). Quantification of Western blot signals (right). **c**, Overlap of STAT3 and p300 binding sites in G14.5 β-cells. **d** Composite plots (upper) and signal intensity (bottom) of p300 at 2,888 STAT3 cobinding sites in (**c**) with increased p300 levels at G14.5 (fold change ≥ 1.2). **e** Signal intensities of H3K27ac at the loci in (**d**). Paired two-sided Wilcoxon rank-sum test. **f**, Western blots of p300 immunoprecipitation eluates from G14.5 islets. 3 biological replicates were performed. **g** Box scatter plots showing β-cells arranged by pseudotime values. **h** Immunofluorescence images of Ki67 and PDX1 in pancreas (left). Scale bar = 50 μm. Quantification of Ki67$^+$PDX1$^+$ cells in all PDX1$^+$ β-cells (right). **i** Immunohistochemistry for insulin (brown) shows β-cell area in pancreatic section (left). Scale bar = 1 mm. Statistics of the β-cell mass in each pancreas (right). **j**, In vivo GSIS levels of mice before and after glucose injection. **k** Comparison of H3K27ac levels between G18.5 WT and G18.5 *Stat3*βKO β-cells. Cyan and pink dots represent the peaks with decreased and increased H3K27ac levels in G18.5 *Stat3*βKO β-cells compared to G18.5 WT β-cells, respectively (p-value ≤ 0.2). Two-sided moderated t-test. **l**, Immunoblot assays of Ins1-RFP$^+$ β-cells from islets cultured under different conditions (left). Quantification of Western blot signals (right). Prolactin concentration: 500 ng/mL. **m**, Box scatter plots showing β-cells cultured under different conditions arranged by pregnancy-associated pseudotime values. Nif: nifuroxazide. Box plots in (**e**, **g, m**) display the median (middle line), 25th–75th percentiles (box), whiskers extending 1.5 times the interquartile range from the edges, minimum and maximum values at whisker ends, unpaired two-sided Wilcoxon rank-sum test was used. n represents the number of mice (**h-i**) or the biological replicates (**b, 1**). Data in (**b, h–j, l**) are presented as mean ± SEM, unpaired two-tailed t-test was used. n represents biological replicates. Source data (**b, h, i, j, l**) are provided as a Source Data file.

was reduced in G18.5 *Acss2*βKO β-cells (Fig. 5l, Supplementary Fig. 9k), and the downregulated genes displayed lower histone acetylation levels in G18.5 *Acss2*βKO β-cells, whereas there were no detectable changes in histone acetylation levels in the regions associated with the upregulated genes (Supplementary Fig. 9l). These findings indicate that ACSS2 is necessary for regulating histone acetylation and mediating pregnancy-associated gene expression in β-cells.

Although ACSS2 appears non-essential for β-cell adaptation at G14.5, its role becomes critical at G18.5, when metabolic demands are heightened. ACSS2 is required for regulating histone acetylation and β-cell adaptation during pregnancy, and the deficiency of ACSS2 prevents metabolic stress and rescues the impaired β-cell function during pregnancy to some extent.

HFD increases metabolic stress in β-cells during pregnancy

Considering the upregulation of genes related to fatty acid metabolism during pregnancy (Fig. 1f) and the induction of glucose intolerance in mice exposed to a high-fat, high-sucrose diet during pregnancy, which can be resolved after returning to a SD postpartum[5,6], we aimed to investigate the effect of high energy intake on β-cell adaptation during pregnancy. We fed mice with HFD for 14 days at non-pregnant (G0) and duration of gestation (G0.5-G14.5). For the detection of the postpartum phenotype, the mice were switched to SD at G14.5 and analyzed at P7-NL. GTT results revealed that despite 14 days of HFD causing elevated GTT levels in G0 mice compared to those fed with SD, G14.5 mice exhibited more severe glucose intolerance under HFD (Fig. 6a). However, the worsened phenotype caused by HFD during pregnancy was restored postpartum within P7-NL mice (Fig. 6a). This result provides evidence that the phenotype induced by HFD during pregnancy resolved postpartum.

We performed scRNA-seq on β-cells from G0, G14.5, and P7-NL mice fed an HFD for 14 days and used scRNA-seq data of β-cells from G0, G14.5, and P7-NL mice fed a SD (Fig. 1c) for control analysis (Supplementary Fig. 10a, b; Supplementary Data 2). Excluding cell cycle-related genes, Uniform Manifold Approximation and Projection (UMAP) and 3D PCA revealed that SD and HFD β-cells from both G0 and P7-NL clustered together, whereas G14.5 SD and G14.5 HFD β-cells formed separate clusters (Fig. 6b, Supplementary Fig. 10c). However, SD and HFD β-cells at the same gestational stages did not present significant differences in the pregnancy-associated trajectory (Supplementary Fig. 10c, d).

DEG analysis confirmed that SD and HFD β-cells at G0 or P7-NL had similar expression profiles with only a few differentially expressed genes (Supplementary Fig. 10e, g; Supplementary Data 4). In contrast, G14.5 HFD β-cells showed upregulation of 412 genes and downregulation of only 11 genes, compared to G14.5 SD β-cells (Supplementary Fig. 10f; Supplementary Data 4). GO analysis revealed that the 412 upregulated genes were related to terms associated with robust glucose catabolic processes and metabolic stress, suggesting that HFD during pregnancy increases β-cell metabolic stress, leading to dysfunction (Fig. 6c, Supplementary Fig. 10f; Supplementary Data 3). While upregulated proliferation level was observed in non-pregnant mice following 14 days of HFD, we documented a notable reduction in the proliferation rates in HFD-fed G14.5 mice (Fig. 6d, e). This observation suggests that the severe metabolic stress induced by HFD disrupts the β-cells proliferation during the advanced stages of pregnancy. Thus, the resolution of β-cell state post-pregnancy supports the use of this HFD model as a valid representation of β-cell dysfunction during pregnancy.

To investigate whether the highly expressed genes in G14.5 HFD β-cells were associated with gestation-related chromatin accessibility, we performed ATAC-seq on HFD β-cells at G0 and G14.5 (Supplementary Fig. 10h). We combined these data with ATAC-seq data from SD β-cells at G0 and G14.5 (Supplementary Fig. 4c) and found that the global chromatin state of HFD β-cells at G0 or G14.5 was relatively similar to that of SD β-cells at the corresponding stages (Supplementary Fig. 10i). Focusing on the ATAC peaks associated with 412 upregulated genes in G14.5 HFD β-cells relative to G14.5 SD β-cells, the hierarchical clustering analysis showed that most of the gene-related loci had increased signal intensity at G14.5 SD compared to G0 SD, while 234 gene loci were unaffected by HFD (Fig. 6f, g). From these findings, we conclude that the chromatin loci of the genes upregulated in G14.5 HFD are generally open during pregnancy and that HFD itself did not induce significant dynamic changes in chromatin accessibility.

ACSS2 deficiency rescues HFD-induced β-cell dysfunction during pregnancy

To investigate whether an HFD induced histone hyperacetylation in β-cells, we measured the H3K27ac levels in HFD β-cells (Supplementary Fig. 10h). We found that HFD increased the overall level of H3K27ac in G14.5 β-cells (Fig. 6h). Additionally, genes upregulated in G14.5 HFD β-cells exhibited enhanced levels of H3K27ac (Supplementary Fig. 10j). Furthermore, *Acss2* expression was higher in HFD β-cells than in SD β-cells at G14.5 but not at G0 (Fig. 6i). These findings suggest that ACSS2 promotes HFD-induced gene expression by regulating the histone acetylation levels of related genes.

To test this inference, we deleted *Acss2* in β-cells in mice fed an HFD. We collected SD and HFD *Acss2*βKO β-cells and WT β-cells at G0 and G14.5 for scRNA-seq (Supplementary Fig. 10a, b; Supplementary Data 2). Both UMAP and 3D PCA plots showed that HFD *Acss2*βKO β-cells and WT β-cells at G0 clustered together, whereas at G14.5, HFD *Acss2*βKO β-cells, HFD WT β-cells, and SD WT β-cells were heterogeneously distributed (Fig. 7a, Supplementary Fig. 10k). Hierarchical clustering analysis revealed that the expression profile of HFD *Acss2*βKO β-cells was more similar to that of SD WT β-cells than that of HFD WT β-cells at G14.5 (Fig. 7b). Notably, genes upregulated in HFD β-cells compared to SD β-cells at G14.5 were significantly downregulated in HFD *Acss2*βKO β-cells compared to HFD WT β-cells at G14.5 (Fig. 7b, c). Additionally, the deletion of *Acss2* caused an increased

https://doi.org/10.1038/s41467-025-58322-3

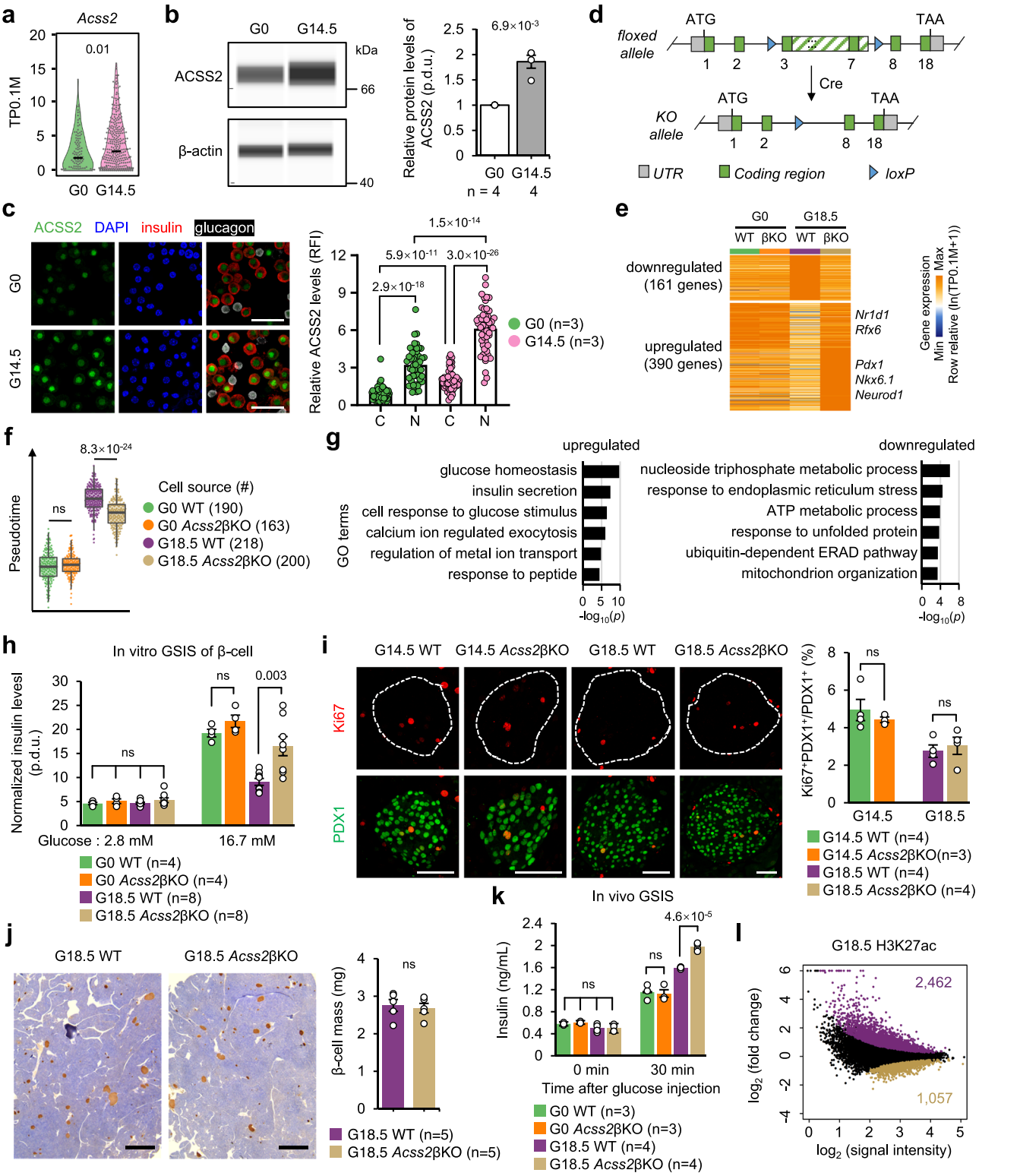

expression of a group of genes in HFD G14.5 *Acss2*βKO β-cells, which included the GO term "potassium ion transport" (Fig. 7b, c; Supplementary Data 3, 4), similar to the results of β-cell function shown in Figs. 5e and 5g. Moreover, H3K27ac CUT&RUN analyses revealed that sites with increased H3K27ac binding in G14.5 HFD β-cells had reduced binding in *Acss2*-deficient β-cells (Fig. 7d, Supplementary Fig. 10h). These findings suggest that *Acss2* deletion may reduce HFD-induced metabolic stress in β-cells during pregnancy and alleviate their dysfunction.

We conducted a series of β-cell function assays and found that the in vitro GSIS capacity of islet β-cells was impaired in HFD G14.5 WT mice compared to SD G14.5 WT mice (Fig. 7e). Remarkably, this impairment was significantly restored in *Acss2*-deficient β-cells at G14.5, but not at G0 (Fig. 7e). Notably, the 14-day of HFD did not exhibit a discernible impact on β-cell mass of G14.5 WT and G14.5 *Acss2*βKO mice (Fig. 7f). Correspondingly, the in vivo GSIS levels were impaired in HFD G14.5 WT mice but significantly increased in HFD G14.5 *Acss2*βKO mice (Fig. 7g). Furthermore, the deficient of *Acss2* significantly

Fig. 5 | ACSS2 promotes β-cell adaptation by regulating histone acetylation. **a** Violin plots showing the expression level of *Acss2* in β-cells. The black line within each violin plot indicates the median expression level. Unpaired two-sided Wilcoxon rank-sum test. **b** Immunoblot assays of Ins1-RFP$^+$ β-cells (left). Quantification of Western blot signals (right). **c** Immunofluorescence images of ACSS2, insulin, and glucagon expression in islet cells (left). Scale bar = 50 μm. Statistical analysis of the relative fluorescence intensity (RFI) of ACSS2 in both the cytoplasm (C) and nucleus (N) of insulin$^+$ β-cells (right). **d** Schematic representation of the generation strategy of an *Acss2-flox* mouse strain. **e** Heatmap showing the expression patterns of the differentially expressed genes between G18.5 WT and G18.5 *Acss2*βKO β-cells (Supplementary Fig. 9e) in four cell populations. Unpaired two-sided Wilcoxon rank-sum test. **f** Box scatter plots showing β-cells arranged by pseudotime values. Box plots display the median (middle line), 25th–75th percentiles (box), whiskers extending 1.5 times the interquartile range from the edges, minimum and maximum values at whisker ends. Unpaired two-sided Wilcoxon rank-sum test. **g** Representative GO terms of upregulated and downregulated genes identified in **f**. Two-sided hypergeometric test. **h**, In vitro GSIS levels of Ins1-RFP$^+$ β-cells in mouse pancreatic islets. **i** Immunofluorescence images of Ki67 and PDX1 expression in (left). Scale bar = 50 μm. Quantification of Ki67$^+$PDX1$^+$ cells in all PDX1$^+$ β-cells (right). **j** Immunohistochemistry for insulin (brown) shows β-cell area in pancreatic sections (left). Scale bar = 1 mm. Statistics of the β-cell mass in each mouse pancreas (right). **k** In vivo GSIS levels of mice before and after glucose injection. **l** Comparison of genome-wide H3K27ac levels between G18.5 WT and G18.5 *Acss2*βKO β-cells. The purple (2,462 peaks) and brown (1,057 peaks) dots represent the peaks with decreased and increased H3K27ac levels in G18.5 *Acss2*βKO β-cells compared to G18.5 WT β-cells, respectively (p value ≤ 0.2). Two-sided moderated t-test. Data in (**b, c, h**–**k**) are presented as mean ± SEM, unpaired two-tailed t test. n represents the number of mice. Source data (**b, c, h**–**k**) are provided as a Source Data file.

mitigated the HFD-induced glucose intolerance in G14.5 mice (Fig. 7h). In the context of HFD, WT mice exhibited increased blood glucose levels at G14.5, whereas the glucose levels of *Acss2*βKO mice were ameliorated (Fig. 7i, Supplementary Fig. 10l).

Therefore, we discovered that HFD exacerbates the metabolic stresses associated with gestation, leading to β-cell maladaptation and impaired function. However, *Acss2*βKO attenuated β-cell exposure to these stresses and rescued β-cell functions.

Discussion

In this study, we delineated the trajectory of adaptive cell state transitions of β-cells during pregnancy using scRNA-seq and multi-omics analysis (Fig. 8a). We identified key regulatory pathways that mediate these transitions, validated by genetic models and single-cell analyses. STAT family proteins were demonstrated to be response factors downstream of lactogen and other hormones[2,43]. Our findings suggest that STAT3 collaborates with p300 to modulate histone acetylation at loci critical for β-cell adaptation. Importantly, we emphasize the potential redundancy between STAT3 and STAT5, particularly in the earlier stages of β-cell adaptation. The enrichment of ACSS2 in the nucleus of β-cells during pregnancy increases acetyl-CoA concentration, which serves as a substrate for histone acetylation reactions (Fig. 8a).

Additionally, our study suggests a mechanism for β-cell dysfunction during pregnancy. Pregnancy-induced extracellular signals, such as prolactin, cause chromatin to become more open, making genes involved in metabolism and β-cell function being more susceptible to environmental influences. If an HFD is consumed during pregnancy, β-cell maladaptation occurs, disrupting metabolic networks and deteriorating β-cell functions, ultimately leading to hyperglycemia (Fig. 8b). Given that STAT3 and p300 regulate a broad range of genes (Supplementary Fig. 5l, 6f, 8h) beyond those related to β-cell pregnancy adaptation, we opted to rescue β-cell function during HFD pregnancy by deleting *Acss2* rather than by inhibiting STAT3 and p300 activities. Our findings imply that limiting energy intake or appropriately suppressing ACSS2 activity in β-cells may prevent the deterioration of β-cell functions during pregnancy. Notably, the specific nuclear localization of ACSS2 in β-cells suggests that ACSS2 deficiency would not significantly affect other acetyl-CoA-associated pathways in the cytoplasm, including mitochondrial function.

Our results demonstrate a marked increase in β-cell proliferation during pregnancy, consistent with existing literatures that highlights significant β-cell expansion as a compensatory response to increased insulin resistance[15,16]. This proliferation is crucial for maintaining overall insulin secretion and glucose homeostasis during pregnancy. Although we observed that the GSIS levels per β-cell significantly decrease during pregnancy, this initially seemed contradictory to reports of increased insulin secretion levels[44]. However, this contradiction is resolved when considering the compensatory increase in β-cell mass, which enhances overall insulin secretion levels during pregnancy.

It is important to note that the timing of phenotype manifestation by knockout of different factors may not be synchronized due to various factors such as protein stability or compensatory effects. In this study, we examined β-cell adaptation at two key time points: G14.5, which represents the peak of β-cell proliferation, and G18.5, which corresponds to the peak of β-cell functional adaptation (Fig. 1b-d). If both physiological and single-cell transcriptomic phenotypes were detectable at G14.5, data were analyzed at this stage; otherwise, we proceeded to G18.5 to capture β-cell adaptation at its peak. Our findings indicate that STAT3 and ACSS2 loss do not have functional effects at G14.5 in SD-fed pregnant mice, despite this being the stage at which β-cell adaptation is initiated. However, the effects of their loss become evident at G18.5, suggesting that their roles in adaptation emerge later in pregnancy. In contrast, β-cell adaptation is already affected at earlier stages (G14.5) in HFD-fed pregnant mice following *Acss2* loss, highlighting the diet-dependent differences in β-cell adaptation mechanisms. These findings suggest that while ACSS2 is dispensable for early adaptation in SD-fed mice, it plays a critical role in adaptation under metabolic stress conditions induced by HFD.

Studies on adaptive changes in β-cells during human pregnancy are extremely limited due to the scarcity of samples. Two studies comparing women at various stages of pregnancy with nonpregnant females of comparable age found a 1.4- to 2-fold increase in β-cell area in the pancreas[45,46], suggesting that β-cell adaptation occurs during pregnancy in humans. To bridge the gap between animal models and potential human clinical implications, we cultured mouse islets with MS and prolactin for four days and observed significant β-cell adaptation (Figs. 3d, e, 4m, Supplementary Fig. 8f). Differences between species, including the duration of pregnancy, suggest that β-cell adaptations during human pregnancy might be regulated by similar epigenetic pathways but acting more gradually, or potentially by different regulatory mechanisms altogether.

Furthermore, we observed augmented expression of genes related to the ER stress response during gestation, a critical factor in the development of T2D[47] (Fig. 1F, Supplementary Fig. 10m). Genes critical to β-cell functionality, such as *Slc30a8*, *Rbp4*, and *Gck*, which have been implicated in T2D and GDM through genome wide association studies findings[48–50], exhibited reduced expression levels during pregnancy (Supplementary Fig 10n). Additionally, our data indicate that HFD intensifies ER stress within β-cells during pregnancy, potentially compromising their function and heightening the risk of GDM. Understanding the mechanisms regulating β-cell adaptation during pregnancy may offer insights into the pathogenic processes associated with both T2D and GDM.

https://doi.org/10.1038/s41467-025-58322-3

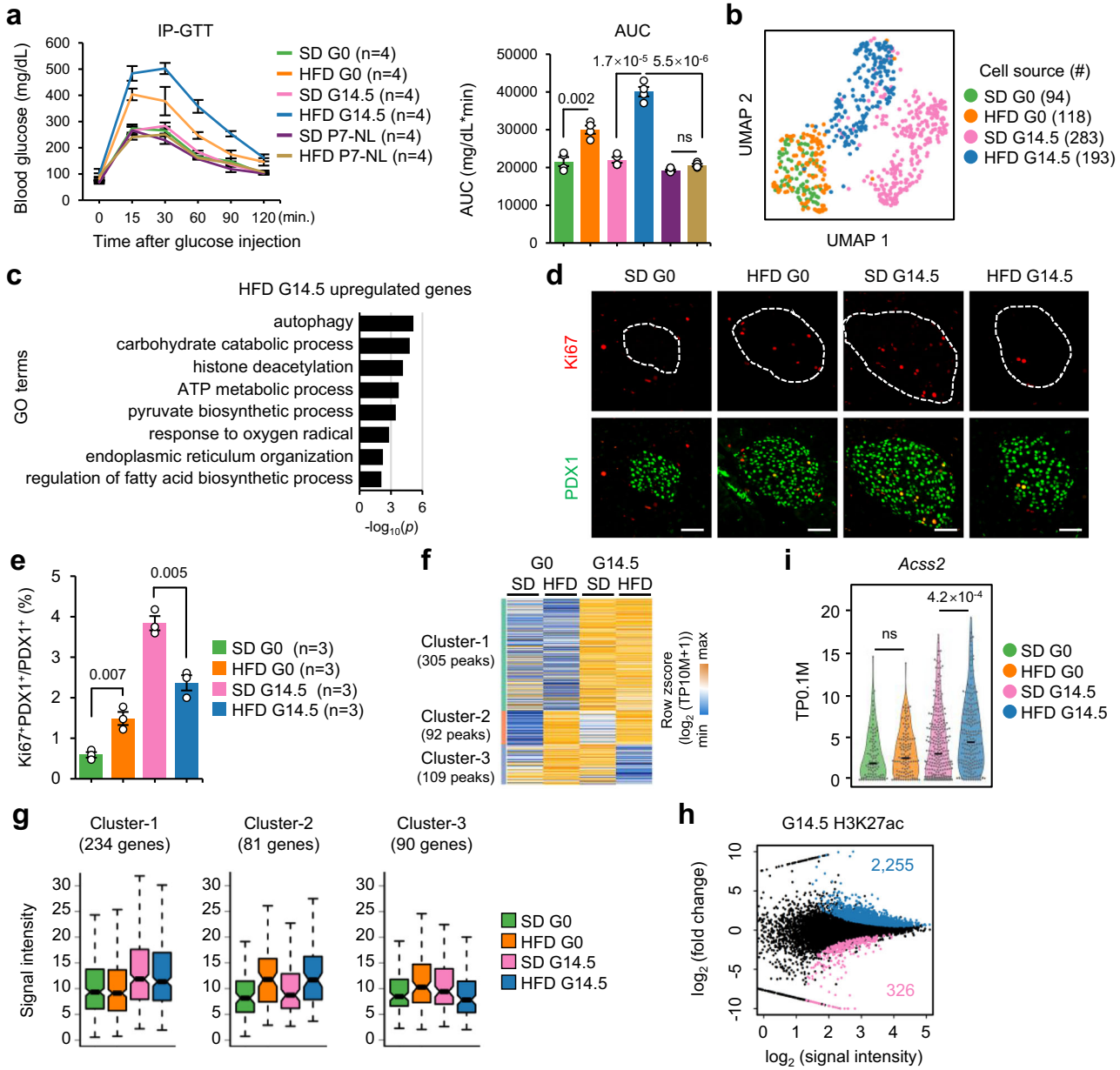

Fig. 6 | HFD increases metabolic stress in β-cells during pregnancy. a IP-GTT levels in fasted mice after glucose injections (left). Quantification of the areas under the curve (AUCs) (right). **b** UMAP plot showing β-cells from different mouse samples. Each point represents a single cell. **c** Selected GO terms enriched among the 412 upregulated genes in HFD G14.5 β-cells (refer to Supplementary Fig. 10f). Two-sided hypergeometric test. **d**, Immunofluorescence images of Ki67 and PDX1 expression in pancreatic tissue sections. Scale bar = 50 μm. **e** Quantification of the percentage of Ki67$^+$PDX1$^+$ cells among all PDX1$^+$ β-cells in each section. More than seven islets and 1,000 PDX1$^+$ cells were counted for each pancreas sample. **f**, Heatmap showing the hierarchical clustering of ATAC-seq signal intensity related to 412 genes highly expressed in HFD G14.5 β-cells (refer to Supplementary Fig. 10f). **g** Box plots of the ATAC-seq signal intensity of the 3 clusters identified in panel **f**. Box plots display the median (middle line), 25th–75th percentiles (box), whiskers extending 1.5 times the interquartile range from the edges, minimum and maximum values at whisker ends. Paired two-sided Wilcoxon rank-sum test. **h** Comparison of genome-wide H3K27ac levels between G14.5 SD and G14.5 HFD β-cells. Each dot represents an H3K27ac CUT&RUN peak. The blue and pink dots represent the peaks with increased and decreased H3K27ac levels in HFD G14.5 β-cells compared to SD G14.5 β-cells, respectively (p value ≤ 0.1). Two-sided moderated t-test. **i**, Violin plots showing the expression levels of *Acss2* in β-cells from different mouse samples. The black line within each violin plot indicates the median expression level. Each point represents a single cell. Unpaired two-sided Wilcoxon rank-sum test. Data in (**a, e**) are presented as mean ± SEM, and unpaired two-tailed t test was used to compare two groups. n represents the number of mice. Source data (**a, e**) are provided as a Source Data file.

The adaptive transition of cells from a physiological to a pathological state is typically a long process, influenced by multiple environmental and genetic variables that complicate its understanding. Our research indicates that the adaptive transition of β-cells during pregnancy in mice can serve as a practical model for investigating the pathophysiology and regulatory mechanisms underlying chronic diseases.

Methods

Mice

All mouse strains used in this study were of the C57BL/6 J background. Mice were housed under temperature-controlled and pathogen-free conditions on a 12 h/12 h light/dark cycle with water available ad libitum. They were provided with either a standard diet (SD) containing 11.3% kcal fat (Xietong Shengwu, 1010044) or a high-fat diet (HFD)

https://doi.org/10.1038/s41467-025-58322-3

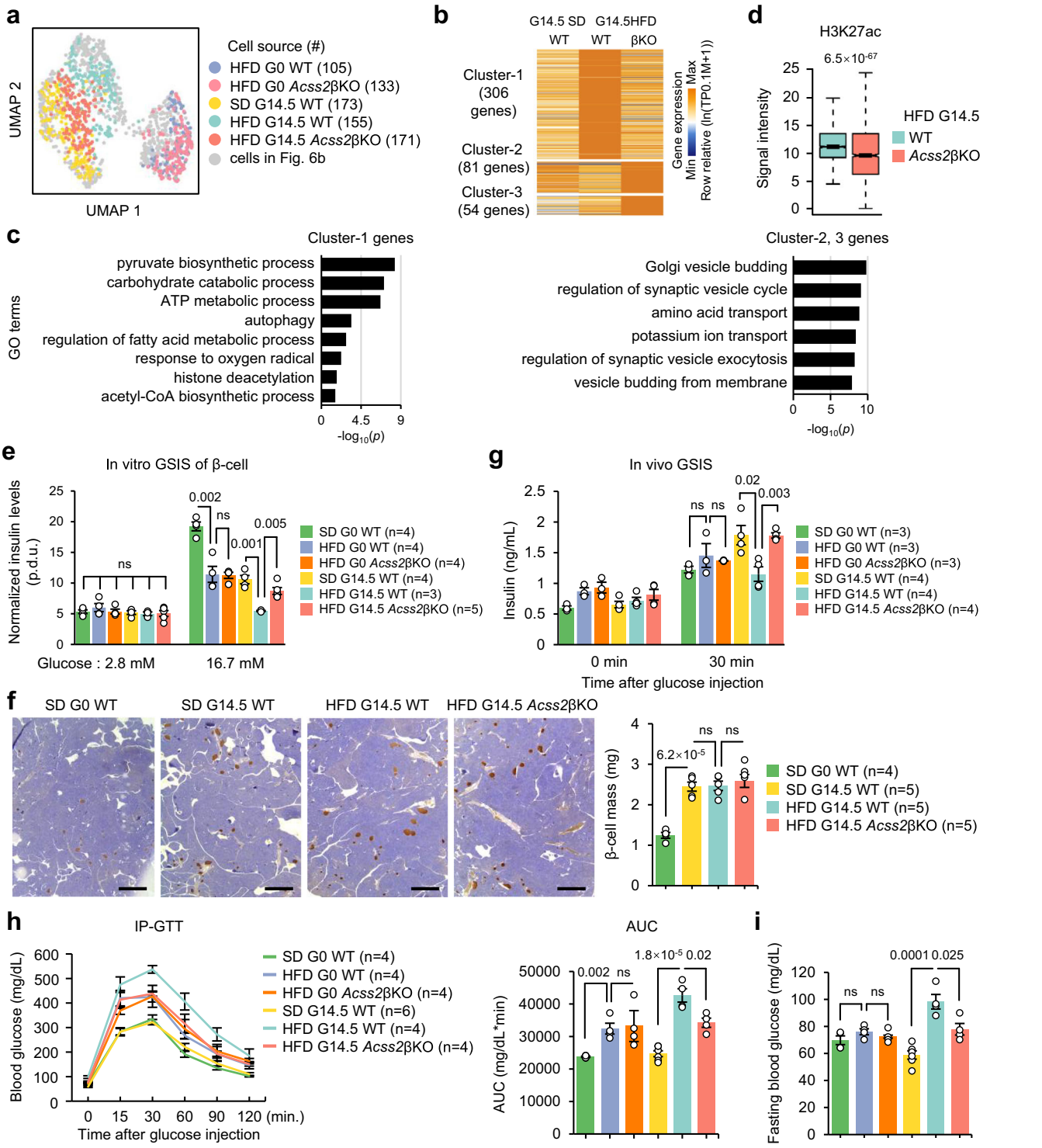

Fig. 7 | ACSS2 deficiency rescues HFD-induced β-cell dysfunction during pregnancy. a UMAP plot showing β-cells from different mouse samples. Each point in represents a single cell. **b** Heatmap showing clusters of a combination of pairwise DEGs among G14.5 SD WT, G14.5 HFD WT, and G14.5 HFD *Acss2*βKO β-cells (p-adjust ≤ 0.01, fold change ≥ 1.5). Unpaired two-sided Wilcoxon rank-sum test. **c** Representative GO terms enriched among the 3 cluster genes in panel (**b**). Two-sided hypergeometric test. **d**, Box plots showing the signal intensity of H3K27ac CUT&RUN at the loci of increased H3K27ac levels in WT G14.5 HFD compared to WT G14.5 SD β-cells in Fig. 6h. Box plots display the median (middle line), 25th–75th percentiles (box), whiskers extending 1.5 times the interquartile range from the edges, minimum and maximum values at whisker ends. Paired two-sided Wilcoxon rank-sum test. 2 Biological replicates were performed (Supplementary Fig. 10h). **e** In vitro GSIS levels of Ins1-RFP^{+} β-cells in mouse pancreatic islets. **f** Immunohistochemistry for insulin (brown) showing β-cell area in pancreatic section (left). Scale bar = 1 mm. Statistics of the β-cell mass in mouse pancreas (right). Eight sections at 100 µm intervals were measured for each pancreas sample. **g** In vivo GSIS levels of mice before and after glucose injection. **h** IP-GTT levels in fasted mice after glucose injections (left). Quantification of the areas under the curve (AUCs) (right). **i**, Fasting (0 min.) blood glucose levels of mice in panel (**h**). Data in (**e-i**) are presented as mean ± SEM, and unpaired two-tailed t test was used to compare two groups. n represents the number of mice. Source data (**e, f, g–i**) are provided as a Source Data file.

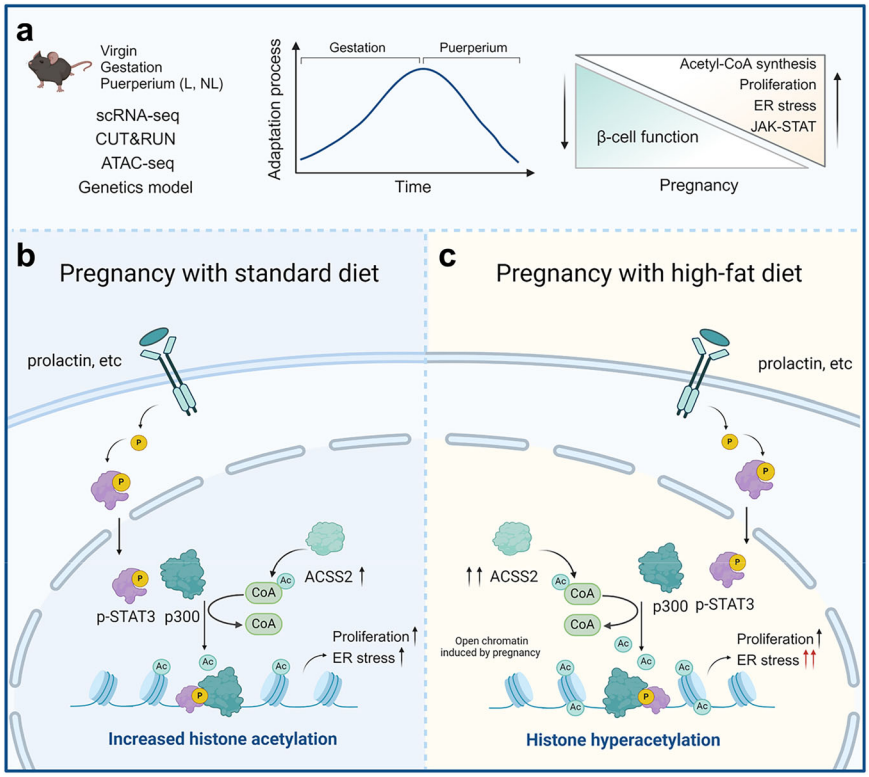

Fig. 8 | Work models of ACSS2 mediating an epigenetic pathway to regulate β-cell adaptation during pregnancy. a Transcriptional profiling, epigenetics, and genetic mouse models are utilized to dissect the processes and molecular features of β-cell adaptation during pregnancy. **b** ACSS2 promotes the increase of acetyl-CoA levels, leading to enhanced histone acetylation and activation of pregnancy-associated genes. This supports β-cell adaptation and function during pregnancy. **c** Under HFD conditions, ACSS2 activity results in hyperacetylation of chromatin and overexpression of metabolic stress-related genes, causing β-cell dysfunction. Illustration created with BioRender (BioRender.com/b01i949).

containing 60% kcal fat (Research Diet, D12492). All animal experiments were approved by the Institutional Animal Care and Use Committee of Peking University.

Mating was confirmed by the presence of a vaginal plug the morning of the next day, which was considered gestation day (G) 0.5. Immediately after delivery, female mice were separated from all pups to establish a nonlactating (NL) mouse model, while lactating (L) mice were left with 7–8 pups. In the G14.5 HFD cohort, the mice were introduced to an HFD commencing at G0.5 and sustained for a duration of 14 days. Mice designated as P7-NL HFD were transitioned to an HFD at G0.5 for 14 days, after which they were reverted to a SD until P7-NL. In the control group, non-pregnant female mice were placed on an HFD for the same 14-day period.

To produce *Acss2*-flox transgenic mice, the CRISPR/Cas9 system was used to insert LoxP elements into the introns between exons 2-3 and between exons 7-8 of the *Acss2-201* transcript, causing a 460 bp interruption in the protein-coding sequence. Deletion of this region causes an open reading frame shift mutation, leading to premature termination of translation and protein mutation. Cas9 mRNA, sgRNA, and donor were microinjected into mouse zygotes, which were transferred into the oviduct of a pseudopregnant mouse to obtain the altered offspring. The offspring were identified by genotyping and sequencing of tail DNA. Genotyping was performed via PCR with the forward primer 5′-TCACTTGAGAACTTCCTACCTTAGCC-3′ and the reverse primer 5′- AGACACTGTGCCCGCTCAACATAT-3′. The sgRNA sequences were 5′-AAGCACGCAACAGGTGCACC-3′ and 5′-GAA-CAGTCTTAGAGATTACC-3′.

Pdx1-Cre^{ER} [34] mice were mated with mice harboring the *p300-flox*[33], *Stat3-flox*[37], or *Acss2-flox* allele. To induce *Cre* recombinase expression in *Pdx1-Cre*^{ER} mice, tamoxifen (Sigma, 13258, 10 mg/mL dissolved in sunflower seed oil) was given by gavage at a dose of 0.1 mg/g body weight one week prior to cohabitation with males. The *Ins1-RFP*[28] mouse strain was crossed for the experiments depicted in Figs. 2–5 and 7, as well as for the in vitro GSIS assay in Fig. 1 and the ATAC-seq and CUT&RUN assays in Fig. 6, to facilitate sorting of β-cells by FACS for subsequent analyses. All the mice used in this study lacked the *GH* minigene, which has been shown to induce ectopic serotonin production.

Human serum preparation

Human serum was obtained from women in the third trimester (> 28 weeks) of pregnancy and age-matched nonpregnant women. All donors provided written informed consent at Shijingshan Hospital in Beijing, China, and were free of diabetes. Approximately 2–4 mL of venous blood was collected from each donor according to a protocol approved by the Peking University Institutional Review Board (PU-IRB) (certificate# IRB00001052-19153). Blood samples were kept on ice for 2 hours (h). After centrifugation at 300 *g* for 5 min at 4 °C, the supernatant was collected and stored at -80 °C.

Single pancreatic islet cell preparation

Pancreatic islets were isolated as previously described[51]. Briefly, the pancreatic tissue was perfused with 0.5 mg/mL collagenase P (Roche, 11213873001) dissolved in 1× HBSS buffer containing 10 mM HEPES (pH 7.4), 1 mM $MgCl_2$, and 5 mM glucose. Digestion was terminated by adding cold PBS. Islets were collected manually and dissociated into a single cell suspension with 0.25% trypsin (Thermo Fisher Scientific, 25200114) and incubated for 3-5 min at 37 °C. Digestion was terminated by adding fetal bovine serum (FBS) (40% vol/vol). After centrifugation at 300 *g* for 5 min at 4 °C, the supernatant was removed, and the cell pellet was resuspended in HBSS buffer. Cells were directly sorted using a BD Aria SORP flow cytometer.

Culture of mouse pancreatic islets

Mouse islets were harvested manually and cultured in RPMI1640 medium (Gibco, 21870076) supplemented with 20% human serum and 1% penicillin/streptomycin. The cultures were treated with 5 μM A485 (Selleck, S8740), 20 μM nifuroxazide (Selleck, S4182), or vehicle (DMSO). The islets were incubated at 37°C with 5% CO_2 for 4 days. Approximately 40 mouse islets per well were seeded in low-adhesion plates, and the medium was changed every 2 days.

ScRNA-seq experiments

For droplet-based scRNA-seq, cDNA preparation and library construction were conducted using the Single Cell 3′ Reagent Kit v3 (10x Genomics) according to the manufacturer's instructions. The libraries were sequenced using an Illumina HiSeq 4000 system to obtain 150 bp paired-end reads.

For Smart-seq3, the procedure was performed according to a published procedure[19]. Briefly, single cells were sorted into 384-well plates containing 0.3 μL of lysis buffer. The mRNA was reverse transcribed into cDNA using 0.1 μL dispensed RT mix. Libraries were constructed using the TruePrep DNA Library Prep Kit (Vazyme, TD501) and sequenced using MGIseq-2000 or Illumina NovaSeq 6000 platforms.

RT–qPCR

Single-cell reverse transcription quantitative PCR (RT–qPCR) was performed with AceQ qPCR SYBR Green Master Mix (Vazyme, Q121-02) on a LightCycler 480 Instrument II (Roche). For bulk-cell qPCR, total RNA was extracted from sorted Ins1-RFP$^+$ β-cells using Pure Micro Kit (DP420, Tiangen). First-strand cDNA was synthesized using HiScript II Q RT SuperMix (R223, Vazyme). The primer sequences used were as follows:

Actb: forward, 5′-TCCTGAGCGCAAGTACTCTGT-3′;
Actb: reverse, 5′-CTGATCCACATCTGCTGGAAG-3′.
Ovol2: forward, 5′-AAAAGCAGAGGAGAGACGCC-3′;
Ovol2: reverse, 5′-ATGTGACCTCAGCCACCAAG-3′.
Ttr: forward, 5′-ACAAGATCCTCACAAGATGGC-3′;
Ttr: reverse, 5′-GGACAGCATCCAGGACTTTGA-3′.
Chgb: forward, 5′-TGTTCCAACGATCACCCCTG-3′;
Chgb: reverse, 5′-GGAGGGACGGAGACTCTCTT-3′.
p300: forward, 5′- CAGCAGCTCAGCCATCTAGTA-3′;
p300: reverse, 5′- TGTCCCCTTCCACTTTACGA-3′.

CUT&RUN and ATAC-seq

CUT&RUN was performed following the previously published protocol[31]. Histone modification CUT&RUN with primary antibodies against H3K27me3 (Millipore, Cat# 07-449, Lot# 2194165, dilution: 1:100), H3K4me1 (Millipore, Cat# 07-436, Lot# 3120573, dilution: 1:100) and H3K27ac (Active motif, Cat# 39133, Lot# 28518012, dilution: 1:100) were performed using 4,000 Ins1-RFP$^+$ cells, while STAT3 and p300 CUT&RUN with primary antibodies against STAT3 (CST, Cat# 12640, Lot# 4, dilution:1:50) and p300 (CST, Cat# 54062, Lot# 62019, dilution:1:50) were performed using 30,000 cells. Each CUT&RUN experiment was performed in at least two biological replicates. CUT&RUN DNA libraries were constructed using the KAPA Hyper Prep kit (Roche, kk2602) and subjected to 150 bp paired-end sequencing on the Illumina NovaSeq 6000 platform.

The miniATAC-seq libraries were prepared using 1,000 Ins1-RFP$^+$ cells following a previously described protocol[52]. ATAC DNA libraries were constructed using the TruePrep DNA Library Prep Kit V2 for Illumina (Vazyme, TD502) and subjected to 150 bp paired-end sequencing on the Illumina NovaSeq 6000 platform.

Western blot assay and capillary-based immunoassays

For the conventional Western blot assay, whole islets were lysed in RIPA buffer (Thermo Scientific, 89900) supplemented with protease inhibitor cocktail. Protein lysates were loaded onto 10% SDS-PAGE gels for separation. Densitometry of the unsaturated bands was performed using Image software (v1.52a). The uncropped and unprocessed scans were provided in the Source Data file.

For immunoblot assay using capillary electrophoresis system, Ins1-RFP$^+$ β-cells were sorted and lysed. Protein concentrations were measured using the BCA protein assay (Bioss, C05-02001). Equal amounts of protein lysate were loaded and separated by WES capillary electrophoresis system (ProteinSimple). Image processing and subsequent quantitative analysis were conducted using Compass for SW software (v6.0.0). Relative protein levels were normalized to the β-actin loading control.

Primary antibodies included anti-Histone H3 (Abcam, Cat# ab1791, Lot# GR177884-2, dilution: 1:1,000), anti- acH3 (Active Motif, Cat# 39139, Lot# 28612004, dilution: 1:1,000), anti-H3K27ac (Active Motif, Cat# 39133, Lot# 01518010, dilution: 1:500), anti-H3K9ac (Abcam, Cat# ab10812, Lot# GR68135-1, dilution: 1:1,000), anti-ACSS2 (T.407.4) (Thermo Scientific, Cat# MA5-14810, Lot# UB2722651, dilution: 1:100), anti-STAT3 (CST, Cat# 12640, Lot# 4, dilution: 1:100), anti-p-STAT3 (Ser727) (CST, Cat# 9134, Lot# 21, dilution: 1:50), and anti-β-ACTIN (ABclonal, Cat# AC026, Lot# UB2722651, dilution: 1:50).

Co-immunoprecipitation assay

For the co-immunoprecipitation (co-IP) assay, anti-p300 antibody (CST, 54062) was incubated with protein complexes in lysis buffer (50 mM Tris-HCl (pH 7.4), 150 mM NaCl, 1 mM EDTA, 1% NP-40, and 0.1% SDS) supplemented with a protease inhibitor cocktail and a phosphatase inhibitor cocktail. Precleared Protein A Dynabeads (Invitrogen, 10002D) were added to the lysate and incubated overnight at 4 °C with gentle agitation. The input protein and coimmunoprecipitation eluates were then used for Western blot assays.

Immunofluorescence staining

Pancreatic tissue was fixed overnight in 4% paraformaldehyde at 4 °C, paraffin-embedded, and sliced into 6 μm thick sections. The sections were rehydrated, autoclaved in antigen unmasking solution (Vector, H-3300) for 10 minutes, and then blocked with TBST (0.1% Tween-20) and 10% FBS. For islet staining, the in vitro cultured islets were directly embedded in OCT and sliced into 20 μm thick sections. For cell staining, islet cells were loaded onto a polylysine-coated slide and fixed with 4% paraformaldehyde at room temperature for 10 minutes. The fixed cells were permeabilized and blocked in PBS containing 0.1% Tween-20 and 5% BSA for 1 hour at room temperature. Primary antibodies used included anti-insulin (Abcam, Cat# ab7842, Lot# GR3317913-1, dilution: 1:400), anti-CHGB (Abcam, Cat# ab12242, Lot# GR3248524-3, dilution: 1:400), anti-PDX1 (Abcam, Cat# ab47383, Lot# GR3199331-1, GR16180-1, dilution: 1:1,000), anti-Ki67 (Abcam, Cat# ab15580, Lot# GR300154-2, dilution: 1:500), anti-H3K27ac (Active motif, Cat# 39133, Lot# 28518012, dilution: 1:400), anti-STAT3 (CST, Cat# 12640, Lot# 4, dilution: 1:500), anti-ACSS2 (CST, Cat# 3658S, Lot# 2, dilution: 1:500), anti-glucagon (Takara, Cat# M182, Lot# AL32797A, dilution: 1:2,000), anti-Serotonin (Immunostar, Cat# 20080, Lot# 2347001, dilution: 1:400) and NKX6.1 (Novus, Cat# NBP1-49672, Lot# E-1, dilution: 1:500). DAPI was used for nuclear staining. Fluorescence images were visualized with a Lecia TCS SP8 or Zeiss AxioImager M2 microscope. Quantification of fluorescence intensity was performed using ImageJ software (v1.52a). For proliferating β-cells (Ki67$^+$PDX1$^+$) cells quantification, we analyzed more than seven islets and 1,000 PDX1$^+$ cells per pancreas. Data for each biological replicate was derived from an individual mouse.

Immunohistochemistry staining and β-cell mass analysis

For the β-cell mass analysis, the pancreas was dissected, weighted and fixed overnight in 4% paraformaldehyde at 4 °C, followed by paraffin-embedded. Intermittent paraffin-sections with a thickness of 10 μm were obtained at 100 μm intervals. Eight sections were stained for

insulin to measure the β-cell area for each pancreas sample. Immunohistochemistry staining was performed using the ABC Kit (Vector Labs, PK-4000). Antibodies used included anti-insulin (CST, 3014) and biotinylated anti-rabbit IgG (Vector Labs, BA1100). Insulin-positive β-cell area and pancreas area were measured using ImageJ software (v1.52a). The β-cell mass was calculated by multiplying the relative area of the insulin-positive region by the total pancreas area and the weight of the pancreas. Data for each biological replicate were derived from an individual mouse.

Acetyl-CoA measurement

Isolated mouse islets were immediately frozen in liquid nitrogen and homogenized in a precooled solution (acetonitrile: methanol: water mixture in a ratio of 2: 2: 1). To this, 0.1 M L-glutamic acid-^{15}N,2,3,3,4,4-d5 was added as the internal standard. The homogenate was centrifuged at 12,000 × *g* for 5 minutes at 4 °C, and the supernatant was retained and then dried under a nitrogen stream in a metal bath at 30 °C. The dried residue was reconstituted in ultrapure water and the acetyl-CoA levels were measurement by liquid chromatography-tandem mass spectrometry (LC-MS/MS). The LC-MS/MS were performed on a ACQUITY UPLC MS/MS system (I-Class TQ-S micro, Waters, Milford, MA). Chromatographic separation was performed on a InfinityLab Poroshell 120 SB-Aq (2.7 μm, 3.0×150 mm, Waters, Milford, MA). All the data acquisition and processing were performed by MassLynx software (v4.1, Waters, USA). The acetyl-CoA content was calibrated with a standard curve of a freshly prepared gradient-diluted standard. The relative amount of acetyl-CoA was normalized to the total protein content in each sample.

IP-GTT and GSIS assay

For the IP-GTT, mice were fasted overnight for 16 hours before receiving an intraperitoneal injection of 20% glucose at a dose of 2 mg/g body weight. Blood glucose levels were measured from a tail vein sample before (0 min) and at 15, 30, 60, 90 and 120 minutes post-injection. For the in vivo GSIS assay, fasted mice were injected intraperitoneally with 20% glucose at 2 mg/g body weight. Blood samples were collected from the orbital sinus at 0 and 30 minutes post-injection. Blood insulin levels were measured using a Rat/Mouse Insulin ELISA kit (Merck Millipore, EZRMI-13K). Non-fasting blood glucose levels were measured in mice at a fixed time between 9:00 and 10:00 am.

For the in vitro GSIS assay, 10 islets of similar volume were picked and preincubated in RPMI1640 medium (Gibco, 21870076) supplemented with 10% FBS and 1% penicillin/streptomycin in a humidified incubator with 5% CO_2 at 37°C for 6 hours. After equilibration, the medium was replaced with Krebs–Ringer bicarbonate (KRB) buffer containing 0.5% bovine serum albumin and 2.8 mM glucose for 1 hour. The preincubation buffer was then replaced with KRB buffer supplemented with different concentrations of glucose (basal: 2.8 mM, stimulatory: 16.7 mM). After 1 hour of incubation, the supernatant was collected. The islets were then digested into single-cell suspensions, and the Ins1-RFP$^+$ β-cell counts were determined using flow cytometric analysis. Insulin levels in the supernatant were measured using a Rat/Mouse Insulin ELISA kit (Merck Millipore, EZRMI-13K). The insulin secretion levels of isolated islets were renormalized to the total number of Ins1-RFP$^+$ β-cells. Data for each biological replicate were obtained from at least three experimental replicates.

Preprocessing of 10x Genomics scRNA-seq data

ScRNA-seq data were processed by the Cellranger toolkit (v3.1.0; 10x Genomics) with default settings. Gene expression values were presented as transcripts per 10 K (TP10K), defined as the ratio of UMI counts per gene to the total UMI in the cell, multiplied by 10,000. These values were then log-transformed by ln (TP10K + 1) for all scRNA-seq analyses throughout the study. 10x Genomics samples with more than 1,500 detected genes (TP10K > 0) and a mitochondrial UMI proportion below 10% were retained for further analysis.

Preprocessing of Smart-seq3 scRNA-seq data

We trimmed the index, primer, and adapter sequences in the paired-end reads with Trimmomatic (v0.39)[53]. The trimmed reads were aligned to the *Mus musculus* reference genome (GRCm38/mm10) using Hisat2[54] (V2.1.0) with the default parameters. Reads were assigned to genes using featureCounts (v2.0.1)[55] with default parameters. Gene expression values were calculated as transcripts per 0.1 million (TP0.1 M) and log-transformed. Protein-coding genes were retained for further analyses. To avoid transcriptome perturbations caused by individual highly expressed genes, the extremely highly expressed hormone genes *Ins1* and *Ins2* were excluded when calculating total transcripts. Only cells in which more than 6,000 genes were detected (TP0.1 M > 0) were retained for further analyses.

Doublet identification and cell type definition for 10x Genomics scRNA-seq data

We modified the DoubletFinder algorithm to identify doublets[56]. Briefly, Doublet identification was conducted by sampling 10% of cells twice to create artificial doublets, merging them, and applying PCA with the Seurat pipeline. In PCA space, a cell's doublet index was determined by the proportion of artificial doublets among its nearest 1% of cells. Cells with the highest 10% of doublet indices were labeled as putative doublets. For each sample, we excluded multihormonal cells, mainly *Ins*$^+$*Sst*$^+$, *Ins*$^+$*Gcg*$^+$, *Gcg*$^+$*Ppy*$^+$, and *Gcg*$^+$*Sst*$^+$ cells, as well as other doublets based on Louvain clustering results using the *FindNeighbors*/*FindClusters* functions in the R package Seurat (v3.2.3)[57].

Cell type identification was performed using the R package Seurat (v3.2.3). We selected the top 2,000 highly variable genes (HVGs) using the *FindVariableFeatures* function with the parameters "selection.method = 'vst'" to construct a pairwise ρ_p matrix. These HVGs were further filtered using the following criteria: coexpressed with at least 5 other HVGs ($\rho_p > 0.15$); detected in at least 0.5% but no more than 90% of total cells; and not a cell cycle-related gene. The remaining coexpressed genes were subjected to PCA using the *RunPCA* function. Then, t-SNE using the *RunTSNE* function and Louvain clustering using the *FindNeighbors*/*FindClusters* function were performed to define cell clusters, which were annotated according to marker gene expression levels.

Identification of proliferative cells from 10x Genomics scRNA-seq data

The top 2,000 HVGs in β-cells were identified using the *FindVariableFeatures* function of the R package Seurat (v3.2.3). Cell cycle-related genes were identified through hierarchical clustering and annotated with Gene Ontology (GO) enrichment analysis. Based on these cell cycle-related genes, we performed hierarchical clustering and Louvain clustering to identify proliferative cells in the β-, α-, δ-, and PP-cell populations.

Identification of β-cell subtypes from Smart-seq3 scRNA-seq data

We applied the R package Seurat (v3.2.3) to identify β-cell subtypes. Initially, we excluded multihormonal cells and non-β-cells from our analysis. The top 2,000 HVGs were identified using the *FindVariableFeatures* function. We then excluded cell cycle-related genes, proto-oncogenes such as *Junb*, *Jun*, and *Fos*, and genes specifically expressed in other cell types, which could be present due to ambient RNA contamination or index switching.

Next, we constructed a pairwise ρ_p matrix of the retained HVGs and further filtered genes using the following criteria: coexpressed with at least 10 other HVGs ($\rho_p > 0.15$) and detected in at least 1% of

total cells. We performed PCA and Louvain clustering on the retained HVGs, which identified *Glut2*^{high} and *Glut2*^{low} β-cell populations.

To identify subpopulations within *Glut2*^{high} or *Glut2*^{low} β-cells, we applied a similar procedure for further cell clustering of the two populations. Proliferative cells were identified by hierarchical clustering using cell cycle-related genes (loading genes of PC1 in Supplementary Fig. 3d).

Differential gene expression analysis

Differentially expressed genes (DEGs) were identified using the *FindMarkers* function of the Seurat package (v3.2.3), with parameters: test.use = "wilcox", pct.1 or pct.2 ≥ 0.3.

GO and KEGG enrichment analysis

We used the R package clusterProfiler (v3.14.3)[58] and Broad Institute GSEA software (v4.1.0)[59] to identify KEGG pathway terms and GO biological process (BP) terms. For GSEA, in brief, the list of expressed genes (expressed in at least 10 cells (TP0.1 M > 1), excluding contaminating genes and cell cycle-related genes) was ranked by the correlation coefficients with pseudotime. Preranked GSEA was performed using 1,000 permutations along with the GO and KEGG gene sets in the Molecular Signatures Database (MSigDB; v7.5.1)[60].

Analysis of the β-cell adaptation trajectory during pregnancy

For *Glut2*^{high} β-cells, Principal Component Analysis (PCA) was performed using the *RunPCA* function in R package Seurat (v3.2.3). The analysis was based on the selected coexpressed genes from the top 2,000 HVGs. The criteria for selection included genes coexpressed with at least 10 other HVGs ($\rho_p > 0.2$) and detected in at least 1% of total cells, while excluding genes causing batch effects.

A second round of PCA was conducted using selected coexpressed genes with the same criteria but excluding cell cycle-related genes. The first two coordinates of the PCA space (PC1 and PC2) were utilized to quantify pseudotime value. For each time point, the gravity center was calculated based on the PC1 and PC2 coordinates. The direction representing the principal variance of the gravity centers was identified with linear regression, and the pseudotime value for each cell was calculated as the inner product between the coordinate and the unit vector along the regressed direction.

To identify pseudotime-related genes, we performed a linear regression between the pseudotime values and ln (TP0.1 M + 1) values for each expressed gene, excluding cell cycle-related genes, proto-oncogenes, genes specifically expressed in other cell types, and genes expressed in fewer than 10 cells. Genes with coefficients p values < 10^{-28} were selected as pseudotime-related genes, which were then clustered using hierarchical clustering analysis.

For *Glut2*^{low} β-cells, a similar procedure was applied, and the pseudotime was measured using the PC2 axis values in Supplementary Fig. 3i.

ScRNA-seq analysis of β-cells from genetically manipulated mice, HFD mice, and culture systems

For β-cells from genetically manipulated or HFD mice, we utilized PCA/UMAP or diffusion mapping. These analyses were performed using the *RunPCA*/ *RunUMAP* function in R package Seurat (v3.2.3) or the *diffuse* function in R package diffusionMap (v1.2.0), respectively. The analyses were based on the top 2,000 HVGs, excluding cell cycle-related genes, proto-oncogenes, and genes specifically expressed in other cell types. Gravity centers of the cell populations were calculated using the coordinates of the first 4 PCs. The principal variance direction of the gravity centers was determined through linear regression. The distance from the start of the regression line to the projection of each cell on the line was calculated as the pseudotime value.

To determine the pregnancy-associated pseudotime values, we used WT G0 and G14.5 (or G18.5) cell populations. For *p300*βKO-related pseudotime values, we used WT G0 and G0 *p300*βKO cell populations. To identify *p300*βKO-related genes in Supplementary Fig 6f, we performed a linear regression between *p300*βKO-related pseudotime values and ln (TP0.1 M + 1) values for each expressed gene, excluding contaminating genes, cell cycle-related genes, proto-oncogenes, and genes expressed in fewer than 10 cells. Genes with coefficients p values < 10^{-11} were subjected to hierarchical clustering.

For β-cells from the culture systems, the TP0.1 M values were normalized by size factors calculated using DESeq (v1.38.0)[61]. Cultured cells were projected onto the PCA plot in Fig. 1c based on the same HVGs. Linear regression was performed to determine the direction of the principal variance representing the gravity centers of the cell populations in Fig. 1c, and the pseudotime values were calculated as described above. To generate the PCA plots shown in Supplementary Fig. 5k, 8g, we selected coexpressed genes (coexpressed with at least 10 other HVGs ($\rho_p > 0.2$) and detected in at least 3% of total cells) from the top 2000 HVGs. PCA was then performed based on the retained coexpressed genes using the *RunPCA* function in the R package Seurat (v3.2.3).

Preprocessing of CUT&RUN and ATAC-seq data

The quality of CUT&RUN and ATAC-seq sequencing data (R1 and R2 fastq files) was assessed using FastQC (v0.11.3) with default parameters. The index, primer, and adapter sequences were trimmed using Trimmomatic (v0.38) with the command "java jar trimmomatic-0.38.jar PE -phred33 fasq1.file fastq2.file ILLUMINACLIP: fasta.-file:2:30:10 LEADING:3 TAILING:3 SLIDINGWINDOW:4:15 MINLEN:36". The trimmed fastq data were aligned to the reference genome mm10 using Bowtie2 (v2.2.5)[62] with default parameters. Only reads with a mapping quality ≥ 30 were retained for further analysis using SAMtools (v1.3.1)[63]. Duplicate PCR reads were excluded using the command "samtools sort in.bam|samtools rmdup -s -out bam". For downstream analyses, we used Homer (v4.6)[64] to calculate tags per 10 million (TP10M) values with the parameters "makeUCSCfile out_dir –o out.bdg –name sample_name –fragLength 150 –avg -fsize 1e20" and stored the resulting data in bedGraph format.

Analyses of CUT&RUN and ATAC-seq data

Define peak sets. The peaks for H3K27ac, H3K4me1, STAT3, p300 CUT&RUN, and ATAC-seq were called using MACS (v1.4.2)[65] with the parameter "-p 1e-3". The peaks of biological replicates were merged by mspc (v4.0.1)[66] with the settings "-m Highest -r bio -c 2 -w weak_pval (H3K27ac, H3K4me1, p300 and ATAC-seq: 1e-5; STAT3 CUT&RUN: 1e-3) -s stringency_pval (H3K27ac, H3K4me1and STAT3 CUT&RUN and ATAC-seq: 1e-8, p300 CUT&RUN: 1e-10) -o out.dir". Regions overlapping with ENCODE blacklisted genomic regions[67] or located in the mitochondrial or Y chromosome were excluded from the subsequent analyses. The average signal intensities of ATAC-seq, H3K4me1, H3K27ac, H3K27me3, p300, and STAT3 in the peak regions were calculated using the *ScoreMatriBin* function of the R package genomation (v1.14.0)[68]. Regions around TSS (±2 kb) were considered promoters, and the start site of the isoform with the highest average chromatin accessibility as the TSS for genes with multiple transcript isoforms. Merged H3K27ac and H3K4me1 peaks located at least 3 kb away from the TSS and H3K4me1 signal intensity ≥ 2.5 at any time point were defined as putative enhancers. The closest gene to a given peak was set as its target gene.

Normalization of average signal intensity. For comparative analysis of H3K27ac under SD and HFD conditions in Figs. 6f, 7d and Supplementary Fig. 10j, we assumed the signal intensities of the closed promoters (promoters not overlapping with ATAC-seq peaks) were approximately the same for each condition. Each signal intensity was normalized by a size factor calculated from the average signal intensity of the closed promoters at the corresponding time point. For STAT3,

which has sharp peaks, the signal intensity was normalized by a size factor calculated from the average signal intensities of the top 350 most highly enriched common peak areas.

Identification of the overlap of H3K27ac and p300, STAT3, and p300 binding sites. The average signal intensities of the merged H3K27ac, p300, and STAT3 peak regions were calculated. Peaks above the threshold signal intensity for each CUT&RUN (H3K27ac: 1.8; p300: 3.0; STAT3: 1.4) were retained.

Differential binding analysis. Differential binding analysis of the CUT&RUN and ATAC-seq data was performed using limma (v3.42.2)[69]. For H3K27ac CUT&RUN of β-cells from knockout or HFD mice, the peaks from biological replicates were merged using mspc (v4.0.1) with the settings "-m Highest -r bio -c 1 -w 1e-5 -s 1e-8". The average signal intensities of the WT/merged H3K27ac peaks below a cutoff value and peak width ≤ 500 bp were discarded for further analyses. The cutoff values for each sample were: G18.5 WT & G18.5 *Stat3*βKO: 3.0; G18.5 WT & G18.5 *Acss2*βKO: 1.8; SD G14.5& HFD G14.5: 3.0.

Motif enrichment analysis of putative enhancers

Motifs were predicted using the "findMotifsGenome.pl" tool with default parameters in Homer (v4.6)[64].

Statistics and Reproducibility

SPSS Statistics Software (v26.0) was used to analyze data for insulin and blood glucose levels, immunostaining, immunochemistry, Western blot signals, and RT–qPCR. These results are presented as mean ± SEM. The number of biological replicates is indicated in the figures. An unpaired two-tailed t-test was used to compare two groups of data, and the p-value was presented in the plot. Not significant (ns), $p \geq 0.05$. For scRNA-seq, CUT&RUN, and ATAC-seq data analyses, the *Wilcox.test* function in R package "stats" (v3.6.3) was used to perform two-sided Wilcoxon rank-sum test for comparing two groups. In the paper, "p-value" for unadjusted comparisons and "p-adjust" for multiple comparisons adjusted using the Benjamini-Hochberg method. At least two biological replicates were performed, as indicated in the t-SNE/PCA plots and the correlation figures. Specific statistical tests for each experiment are described in the figure legends.

Reporting summary

Further information on research design is available in the Nature Portfolio Reporting Summary linked to this article.

Data availability

The CUT&RUN, ATAC-seq, and scRNA-seq data generated in this study have been deposited in the Gene Expression Omnibus (GEO) database under accession code GSE241776. The relevant raw data from figures generated in this study are provided in the Source Data file. Source data are provided with this paper.

Code availability

Please visit https://github.com/ShuangHe33/islet_beta_pregnancy for all code relevant to this project. For any additional requests, please contact authors.

References

1. Sferruzzi-Perri, A. N., Lopez-Tello, J., Napso, T. & Yong, H. E. J. Exploring the causes and consequences of maternal metabolic maladaptations during pregnancy: lessons from animal models. *Placenta* **98**, 43–51 (2020).
2. Banerjee, R. R. Piecing together the puzzle of pancreatic islet adaptation in pregnancy. *Ann. N. Y Acad. Sci.* **1411**, 120–139 (2018).
3. Brănişteanu, D. D. & Mathieu, C. Progesterone in gestational diabetes mellitus: guilty or not guilty? *Trends Endocrinol. Metab.* **14**, 54–56 (2003).
4. Chiefari, E., Arcidiacono, B., Foti, D. & Brunetti, A. Gestational diabetes mellitus: an updated overview. *J. Endocrinol. Investig.* **40**, 899–909 (2017).
5. Park, S. & Kim, S. H. Gestational diabetes is associated with high energy and saturated fat intakes and with low plasma visfatin and adiponectin levels independent of prepregnancy BMI. *Diabetes* **62**, A361–A361 (2013).
6. Pennington, K. A., van der Walt, N., Pollock, K. E., Talton, O. O. & Schulz, L. C. Effects of acute exposure to a high-fat, high-sucrose diet on gestational glucose tolerance and subsequent maternal health in mice. *Biol. Reprod.* **96**, 435–445 (2017).
7. Baeyens, L., Hindi, S., Sorenson, R. L. & German, M. S. beta-cell adaptation in pregnancy. *Diabetes Obes. Metab.* **18**, 63–70 (2016).
8. Schraenen, A. et al. Placental lactogens induce serotonin biosynthesis in a subset of mouse beta cells during pregnancy. *Diabetologia* **53**, 2589–2599 (2010).
9. Zhao, X. et al. Involvement of the STAT5-cyclin D/CDK4-pRb pathway in beta-cell proliferation stimulated by prolactin during pregnancy. *Am. J. Physiol. Endocrinol. Metab.* **316**, E135–E144 (2019).
10. Brelje, T. C., Svensson, A. M., Stout, L. E., Bhagroo, N. V. & Sorenson, R. L. An immunohistochemical approach to monitor the prolactin-induced activation of the JAK2/STAT5 pathway in pancreatic islets of Langerhans. *J. Histochem Cytochem* **50**, 365–383 (2002).
11. Kim, H. et al. Serotonin regulates pancreatic beta cell mass during pregnancy. *Nat. Med* **16**, 804–808 (2010).
12. Layden, B. T. et al. Regulation of pancreatic islet gene expression in mouse islets by pregnancy. *J. Endocrinol.* **207**, 265–279 (2010).
13. Rieck, S. et al. The transcriptional response of the islet to pregnancy in mice. *Mol. Endocrinol.* **23**, 1702–1712 (2009).
14. Chung, J. Y. et al. Pancreatic islet cell type–specific transcriptomic changes during pregnancy and postpartum. *iScience* **26**, 2589–0042 (2023).
15. Karnik, S. K. et al. Menin controls growth of pancreatic beta-cells in pregnant mice and promotes gestational diabetes mellitus. *Science* **318**, 806–809 (2007).
16. Zhang, H. et al. Gestational diabetes mellitus resulting from impaired beta-cell compensation in the absence of FoxM1, a novel downstream effector of placental lactogen. *Diabetes* **59**, 143–152 (2010).
17. Feng, Y. *et al*. Characterizing pancreatic β-cell heterogeneity in the streptozotocin model by single-cell transcriptomic analysis Check. *Mol Metab* **37** (2020).
18. van der Meulen, T. et al. Virgin beta cells persist throughout life at a neogenic niche within pancreatic islets. *Cell Metab.* **25**, 911–926 (2017).
19. Hagemann-Jensen, M., Ziegenhain, C. & Sandberg, R. Scalable single-cell RNA sequencing from full transcripts with Smart-seq3xpress. *Nat. Biotechnol.* **40**, 1452–1457 (2022).
20. Moon, J. H. *et al*. Lactation improves pancreatic beta cell mass and function through serotonin production. *Sci Transl Med* **12** (2020).
21. Back, S. H. & Kaufman, R. J. Endoplasmic reticulum stress and type 2 diabetes. *Annu. Rev. Biochem.* **81**, 767–793 (2012).
22. Yong, J., Johnson, J. D., Arvan, P., Han, J. & Kaufman, R. J. Therapeutic opportunities for pancreatic beta-cell ER stress in diabetes mellitus. *Nat. Rev. Endocrinol.* **17**, 455–467 (2021).
23. Schroder, M. & Kaufman, R. J. The mammalian unfolded protein response. *Annu. Rev. Biochem.* **74**, 739–789 (2005).
24. Hudish, L. I., Reusch, J. E. & Sussel, L. Beta cell dysfunction during progression of metabolic syndrome to type 2 diabetes. *J. Clin. Invest* **129**, 4001–4008 (2019).
25. Sivanand, S., Viney, I. & Wellen, K. E. Spatiotemporal control of Acetyl-CoA metabolism in chromatin regulation. *Trends Biochem. Sci.* **43**, 61–74 (2018).

26. Hughes, E. & Huang, C. Participation of Akt, Menin, and p21 in pregnancy-induced beta-cell proliferation. *Endocrinology* **152**, 847–855 (2011).
27. Jiang, W. J., Peng, Y. C. & Yang, K. M. Cellular signaling pathways regulating beta-cell proliferation as a promising therapeutic target in the treatment of diabetes. *Exp. Ther. Med* **16**, 3275–3285 (2018).
28. Piccand, J. et al. Pak3 promotes cell cycle exit and differentiation of beta-cells in the embryonic pancreas and is necessary to maintain glucose homeostasis in adult mice. *Diabetes* **63**, 203–215 (2014).
29. Rieck, S. & Kaestner, K. H. Expansion of beta-cell mass in response to pregnancy. *Trends Endocrinol. Metab.* **21**, 151–158 (2010).
30. Nitsch, S., Zorro Shahidian, L. & Schneider, R. Histone acylations and chromatin dynamics: concepts, challenges, and links to metabolism. *EMBO Rep.* **22**, e52774 (2021).
31. Skene, P. J., Henikoff, J. G. & Henikoff, S. Targeted in situ genome-wide profiling with high efficiency for low cell numbers. *Nat. Protoc.* **13**, 1006–1019 (2018).
32. Lasko, L. M. et al. Discovery of a selective catalytic p300/CBP inhibitor that targets lineage specific tumours. *Nature* **550**, 128–132 (2017).
33. Kasper, L. H. et al. Conditional knockout mice reveal distinct functions for the global transcriptional coactivators CBP and p300 in T-cell development. *Mol. Cell Biol.* **26**, 789–809 (2006).
34. Gu, G. Q., Dubauskaite, J. & Melton, D. A. Direct evidence for the pancreatic lineage: NGN3$^+$cells are islet progenitors and are distinct from duct progenitors. *Development* **129**, 2447–2457 (2002).
35. Brelje, T. C., Stout, L. E., Bhagroo, N. V. & Sorenson, R. L. Distinctive roles for prolactin and, growth hormone in the activation of signal transducer and activator of transcription 5 in pancreatic islets of Langerhans. *Endocrinology* **145**, 4162–4175 (2004).
36. Lee, J.-Y. et al. The transcription factors Stat5a/b are not required for islet development but modulate pancreatic β-cell physiology upon aging. *Biochim. et. Biophys. Acta (BBA) - Mol. Cell Res.* **1773**, 1455–1461 (2007).
37. Moh, A. et al. Role of STAT3 in liver regeneration: survival, DNA synthesis, inflammatory reaction and liver mass recovery. *Lab Invest* **87**, 1018–1028 (2007).
38. Mews, P. et al. Acetyl-CoA synthetase regulates histone acetylation and hippocampal memory. *Nature* **546**, 381–386 (2017).
39. Pietrocola, F., Galluzzi, L., Bravo-San Pedro, J. M., Madeo, F. & Kroemer, G. Acetyl Coenzyme A: a central metabolite and second messenger. *Cell Metab.* **21**, 805–821 (2015).
40. Chakrabarti, S. K. & Mirmira, R. G. Transcription factors direct the development and function of pancreatic beta cells. *Trends Endocrin Met* **14**, 78–84 (2003).
41. Piccand, J. et al. Rfx6 maintains the functional identity of adult pancreatic beta cells. *Cell Rep.* **9**, 2219–2232 (2014).
42. Vieira, E. et al. The clock gene rev-erb alpha regulates pancreatic beta-cell function: modulation by leptin and high-fat diet. *Endocrinology* **153**, 592–601 (2012).
43. Salazar-Petres, E. R. & Sferruzzi-Perri, A. N. Pregnancy-induced changes in beta-cell function: what are the key players? *J. Physiol.* **600**, 1089–1117 (2021).
44. Ohara-Imaizumi, M. et al. Serotonin regulates glucose-stimulated insulin secretion from pancreatic β cells during pregnancy. *Proc. Natl Acad. Sci.* **110**, 19420–19425 (2013).
45. Butler, A. E. et al. Adaptive changes in pancreatic beta cell fractional area and beta cell turnover in human pregnancy. *Diabetologia* **53**, 2167–2176 (2010).
46. Van Assche, F. A., Aerts, L. & Prins, F. D. A morphological study of the endocrine pancreas in human pregnancy. *BJOG: Int. J. Obstet. Gynaecol.* **85**, 818–820 (1978).
47. Yong, J., Johnson, J. D., Arvan, P., Han, J. & Kaufman, R. J. Therapeutic opportunities for pancreatic β-cell ER stress in diabetes mellitus. *Nat. Rev. Endocrinol.* **17**, 455–467 (2021).
48. Kwak, S. H. et al. A genome-wide association study of gestational diabetes mellitus in Korean women. *Diabetes* **61**, 531–541 (2012).
49. Hu, S. et al. Relationships of SLC2A4, RBP4, PCK1, and PI3K Gene Polymorphisms with Gestational Diabetes Mellitus in a Chinese Population. *Biomed. Res Int* **2019**, 7398063 (2019).
50. Freathy, R. M. et al. Hyperglycemia and Adverse Pregnancy Outcome (HAPO) study: common genetic variants in GCK and TCF7L2 are associated with fasting and postchallenge glucose levels in pregnancy and with the new consensus definition of gestational diabetes mellitus from the International Association of Diabetes and Pregnancy Study Groups. *Diabetes* **59**, 2682–2689 (2010).
51. Li, L. C. et al. Single-cell transcriptomic analyses of mouse pancreatic endocrine cells. *J. Vis Exp* (2018).
52. Wu, J. et al. Chromatin analysis in human early development reveals epigenetic transition during ZGA. *Nature* **557**, 256–260 (2018).
53. Bolger, A. M., Lohse, M. & Usadel, B. Trimmomatic: a flexible trimmer for Illumina sequence data. *Bioinformatics* **30**, 2114–2120 (2014).
54. Kim, D., Langmead, B. & Salzberg, S. L. HISAT: a fast spliced aligner with low memory requirements. *Nat. Methods* **12**, 357–360 (2015).
55. Liao, Y., Smyth, G. K. & Shi, W. featureCounts: an efficient general purpose program for assigning sequence reads to genomic features. *Bioinformatics* **30**, 923–930 (2014).
56. McGinnis, C. S., Murrow, L. M. & Gartner, Z. J. DoubletFinder: doublet detection in single-cell RNA sequencing data using artificial nearest neighbors. *Cell Syst.* **8**, 329–337 (2019).
57. Butler, A., Hoffman, P., Smibert, P., Papalexi, E. & Satija, R. Integrating single-cell transcriptomic data across different conditions, technologies, and species. *Nat. Biotechnol.* **36**, 411 (2018).
58. Yu, G., Wang, L. G., Han, Y. & He, Q. Y. clusterProfiler: an R package for comparing biological themes among gene clusters. *OMICS* **16**, 284–287 (2012).
59. Subramanian, A. et al. Gene set enrichment analysis: a knowledge-based approach for interpreting genome-wide expression profiles. *Proc. Natl Acad. Sci. USA* **102**, 15545–15550 (2005).
60. Liberzon, A. et al. Molecular signatures database (MSigDB) 3.0. *Bioinformatics* **27**, 1739–1740 (2011).
61. Anders, S. & Huber, W. Differential expression analysis for sequence count data. *Genome Biol.* **11**, R106 (2010).
62. Langmead, B. & Salzberg, S. L. Fast gapped-read alignment with Bowtie 2. *Nat. Methods* **9**, 357–359 (2012).
63. Li, H. et al. The sequence alignment/map format and SAMtools. *Bioinformatics* **25**, 2078–2079 (2009).
64. Heinz, S. et al. Simple combinations of lineage-determining transcription factors prime cis-regulatory elements required for macrophage and B cell identities. *Mol. Cell* **38**, 576–589 (2010).
65. Zhang, Y. et al. Model-based analysis of ChIP-Seq (MACS). *Genome Biol.* **9**, R137 (2008).
66. Jalili, V., Matteucci, M., Masseroli, M. & Morelli, M. J. Using combined evidence from replicates to evaluate ChIP-seq peaks. *Bioinformatics* **31**, 2761–2769 (2015).
67. Consortium, E. P. An integrated encyclopedia of DNA elements in the human genome. *Nature* **489**, 57–74 (2012).
68. Akalin, A., Franke, V., Vlahovicek, K., Mason, C. E. & Schubeler, D. Genomation: a toolkit to summarize, annotate and visualize genomic intervals. *Bioinformatics* **31**, 1127–1129 (2015).
69. Ritchie, M. E. et al. limma powers differential expression analyses for RNA-sequencing and microarray studies. *Nucleic acids res* **43**, e47 (2015).

Acknowledgements

We thank Drs. Junqing Ye and Wei-Lin Qiu for critical advice; Dr. Kun Hu for assistance with human blood sample collection; Ms. Yinghua Guo (Flow Cytometry Core) and Ms. Guilan Li (Protein Core) at the National Center for Protein Sciences, Peking University, for technical support; and Dr. Xiaowei Chen, Ms. Yawei Wang, Mr. Li Quan, and Mr. Kunlun

Cheng for assistance with LC–MS/MS experiments. This work was supported by the National Key Research and Development Program of China (2024YFA1802900 and 2023YFA1800600 to C.-R.X.) the National Natural Science Foundation of China (32125014 and 32030034 to C.-R.X., and 32000566 to X.-X.Y.), and funding from the Peking-Tsinghua Center for Life Sciences to C.-R.X.

Author contributions

C.-R.X. conceived the project; C.-R.X. and Y.Z. designed the research; Y.Z., Xi W., M.-Y.H. and X.-X.Y. performed the research; Y.Z., S.H., Xin W. and C.-R.X. analyzed the data; Y.Z., S.H. and C.-R.X. wrote the manuscript.

Competing interests

The authors declare no competing interests.

Additional information

Supplementary information The online version contains supplementary material available at https://doi.org/10.1038/s41467-025-58322-3.

Correspondence and requests for materials should be addressed to Cheng-Ran Xu.

Peer review information *Nature Communications* thanks the anonymous reviewers for their contribution to the peer review of this work. A peer review file is available.